Electronic Supplementary Material (ESI) for Energy & Environmental Science

Oscillating lithium ion-acceptor fluorine-donor electrolyte for practical fast-charging high-energy lithium metal pouch cells

Digen Ruan,[a] Yanru Wang,[b] Jiasen Guo,[a] Zhuangzhuang Cui,[a] Qingshun Nian,[a] Zhihao Ma,[a] Dazhuang Wang,[a] Jiajia Fan,[a] Jun Ma,[a] Bingqing Xiong,[a] Qi Dong,[a] Ruiguo Cao,[a] Shuhong Jiao,[a] and Xiaodi Ren*[a]

a. Hefei National Research Center for Physical Sciences at the Microscale, School of Chemistry and Materials Science, University of Science and Technology of China, Anhui 230026, China.

b. The Instruments Center for Physical Science, University of Science and Technology of China, Hefei, Anhui, 230026, China.

Methods

Materials

The raw materials for synthesis including tetraethylene glycol (TEG), 2-Bromo-1,1-dimethoxyethane (BrDMN) and potassium fluoride (KF) were provided by Macklin, Bidepharm and Aladdin, respectively. 1,2-diethoxyethane (DEE) and 1-dimethoxy-ethan (HDMN) were purchased from Aladdin, while 1,1,2,2-Tetrafluoroethyl-2,2,3,3-tetrafluoropropylether (TTE) was obtained from Shang Fluoro Technology Co., Ltd. All the solvents were dried by 4 Å molecular sieve for more than three days before use. LiFSI was purchased from Dadu New Material Co., Ltd. and dried under vacuum at 100 °C for 24 hours. Thick Li disc (450 μm) and ultra-thin Li foils (20 μm) were supplied by Guangdong Canrd New Energy Technology and China Energy Lithium, respectively. NMC811 cathode slurry with the active particle (poly crystalline NMC811, Hunan Shanshan Energy Technology Co., Ltd.), polyvinylidene fluoride (PVDF) in N-methyl-2-pyrrolidone (NMP) and super P Li conductive carbon was coated on aluminum foil for medium to NMC811 electrodes (loading of 9.0 mg cm^{-2}) and their mass ratio is 90%: 5%: 5% (in weight ratio). NMC622 (highly active polycrystalline particles) sheets were supplied by Guangdong Canrd New Energy Technology, which contained with 96.5% active material (loading of 8.8 mg cm^{-2}). To remove residual solvent and moisture, the electrodes were vacuum dried at 100 ℃ for 12 hours before use.

Synthesis

BrDMN and KF were mixed in a molar ratio of 1: 2, and the reaction solvent TEG was added (in the ratio of 0.1 mol of KF to 25 mL of TEG), and the mixture was then magnetically stirred for 8 hours at 150 °C in an oil bath. After the reaction, the KF solid was filtered off and the resulting filtrate was vacuum distilled (-99 kPa) using 150 °C oil bath to obtain a mixture of BrDMN and FDMN, which was further purified under atmospheric pressure with 130 °C oil bath for more than two times to get a clear colorless liquid of high-purity product FDMN (reaction yield: 21%). The pure product obtained was further transferred to the argon-filled glove box for storage and dried with 4 Å molecular sieves for more than 3 days before use. NMR was employed to characterize the synthesized sample. ^{1}H-NMR (400 MHz, CDCl$_3$, δ/ppm): 4.60 (dt, J = 7.4, 5.2 Hz), 4.35 (dd, J = 46.8, 5.2 Hz), 3.44. ^{13}C-NMR (400 MHz, CDCl$_3$, δ/ppm): 101.47 (d, J = 24.2 Hz), 81.38 (d, J = 171.7 Hz), 54.30. ^{19}F-NMR (400 MHz, CDCl$_3$, δ/ppm): -232.46. HPLC-TOF MS (Acquity UPLC-Xevo G2QTof) is employed for high-resolution molecular weight tests of FDMN and BrDMN. ESI-MS calculated [FDMN+Na+]: 131.0479 and found 131.0460; ESI-MS calculated [BrDMN+Na+]: 190.9679 and found 190.9681.

Electrolyte preparations

The electrolytes were prepared in the argon-filled glovebox (H$_2$O < 0.1 ppm, O$_2$ < 0.1 ppm). The saturated LHCE (Base-DEE) and unsaturated LHCE (E-DEE) consists of LiFSI, DEE and TTE in molar ratios of 1: 1: 3 and 1: 1.5: 3, respectively. The electrolytes named E-HDMN and E-FDMN are composed of LiFSI: DEE: HDMN: TTE=1: 1: 0.5: 3 (molar ratio) and LiFSI: DEE: FDMN: TTE=1: 1: 0.5: 3 (molar ratio), respectively. Similarly, EDMC-DMC, EDMC-HDMN and EDMC-FDMN represent that the components of the electrolytes are LiFSI: DMC: TTE=1:2.7:3, LiFSI: DMC: HDMN: TTE=1: 2.2: 0.5: 3 and LiFSI: DMC: FDMN: TTE=1: 2.2: 0.5: 3 (in molar ratio), respectively. LB002 is the commercial carbonate electrolyte made of 1M LiPF$_6$ in EC:EMC:DMC=1:1:1 (in volume ratio).

Electrochemical measurements

All CR2032 coin cells (Guangdong Canrd New Energy Technology) were assembled using two pieces of Celgard 2500 separator along with three formation cycles (0.5 mA cm^{-2} and 1 mAh cm^{-2}) for Li||Cu and Li||Li cells operated at above 1 mA cm^{-2} while a pieces of Celgard 2500 separator for NMC||Li cells and Li||Cu cells operated at below 1 mA cm^{-2}. The amount of the electrolyte used for each cell is 40 μL. The electrochemical cycling measurements for coin cells were

conducted on Land (CT2001A) and NEWARE Battery Testing System (CT-4008T-5V10mA-164) at room temperature (25 °C). NMC||Li cells were carried out at C/10 rates (1 C = 200 mA g^{-1}) for two formation cycles and cycled at 1 C and 2 C for the following cycled in the voltage range of 2.8-4.5 V. Electrochemical impedance spectroscopy (EIS) were performed in the frequency range from 100 mHz to 1 MHz with an AC amplitude of 5 mV on a Solartron frequency analyzer for the cycled cells. For Li$^+$ transference number measurements, the initial and steady polarization currents I_0 and I_{ss} were tested under a polarization potential of 5 mV for 2000 s. The initial and steady bulk resistances (R_b^0 and R_b^{ss}) and interfacial resistances (R_i^0 and R_i^{ss}) were obtained by EIS before and after the above potentiostatic polarization. The t_{Li^+} was calcuated by the following equation:

$$t_{Li^+} = \frac{I^{ss}R_b^{ss}(\Delta V - I^O R_i^O)}{I^O R_b^O(\Delta V - I^{ss}R_i^{SS})}$$

The 2 Ah-class NMC811||Li pouch cells (dry cell from EVE battery Ltd., details in **Table S4**) were first filled with different electrolytes and controled E/C=1.5 g Ah^{-1}, activated for two cycles using 0.05 C (1 C=2 A) and then cycled under 1 C charge and 2 C discharge in the voltage range of 2.8-4.4 V using NEWARE Battery Testing System (CT-4008Tn-5V12A-S1). Pressure applied to the pouch cells is ~200 kpa.

Material characterizations

Raman spectroscopy for the electrolyte solvation structure was performed on Horiba LabRAM HR Evolution microscope with a 785 nm excitation laser, and ^{7}Li-NMR was conducted by 600 MHz Brooke. The details of ^{7}Li-^{19}F two-dimensional (2D) heteronuclear overhauser effect spectroscopy (HOESY) NMR test are the same as the previous work.[1] To characterize the electrodes, the cycled cells were first disassembled in the glove box and then the collected electrodes were washed using DME at least three times to remove the remaining electrolyte. At last, the obtained electrodes were dried in vacuum. X-ray photoelectron spectroscopy (XPS, 250XI ESCALAB Thermo Fisher Scientific) was used to test the interfacial components of the cycled electrodes with different electrolytes. TEM (FEI-Talos F200x, U.S.) was employed to examine the CEI films of NMC622. A Gemini SEM 450 microscope was applied to characterize the NMC622 samples, while a Tungsten Hairpin Filament SEM characterizes the Li samples. For cryo-TEM measurement, the copper TEM grids were removed from cycled Li||Cu cells using different electrolytes (3 mA cm^{-2} with deposition capacity of 0.05 mAh cm^{-2}) and were rinsed with DME in an argon-filled glove box. Cryo-TEM characterization was carried out on JEOL-F200 equipped with a cryo transfer holder (Gatan 698) and an electron energy loss spectrum system (Gatan 1065 IS). A cryo-transfer box was used to isolate water and oxygen throughout the sample installation. The dewar tank of the holder maintained the sample at -179 ℃ during the sample transfer and TEM observation, which helped to protect the electron damage. All the characterizations including HRTEM, HAADF, EDS and EELS analysis of SEIs were collected at 200 kV and low electron flux. The cryo-TEM data were analyzed using the Gatan Microscopy Suite software, and applying masks (smooth edge: 5 pixels) to the crystal signals obtained in the FFT images.

Theoretical calculations

Quantum chemistry calculations were first performed to optimize molecular geometries of DEE, HDMN, FDMN, DFDMN, TFDMN and TTE molecules using the Gaussian 16 package at B3LYP/6-311+G(d,p) level of theory.[2] The binding energy was calculated using the equation from our previous work.[1] The adsorption energy via DFT calculations involving geometry optimization, energy calculations, and electronic properties are performed with the Vienna Ab initio simulation package (VASP). The projector-augmented wave (PAW) potentials with OTFG ultrasoft pseudo-potential and

generalized gradient approximation of Perdew-Burke-Ernzerhof (GGA-PB) are employed. The cutoff energy of 500 eV was determined through convergence testing. To prevent interaction between adjacent surfaces, a vacuum region of 30 Å was introduced, and the Brillouin zone was sampled with 5×5×1 k-points to ensure that the spacing along the axial direction in reciprocal space was approximately equal to 0.02 Å^{-1}. The structures were fully relaxed until the forces reached a threshold of 0.01 eV, and self-consistent convergence was achieved at a level of 5×10^{-6} eV per atom. In modeling the interface, the anode is the (200) crystalline Li metal, while the cathode is the Li-deficient state of NiO.

The atomic partial charges on these solvent molecules were computed by fitting to the molecular electrostatic potential at atomic centers with the Møller-Plesset second-order perturbation method and the correlation-consistent polarized valence cc-pVTZ(-f) basis set. The atomistic force field parameters for all ions and molecules are described by the General Amber Force Field (GAFF) format and are taken from previous work.[3] The cross-interaction parameters between different atom types are obtained from the Lorentz-Berthelot combination rule. Atomistic simulations were performed using GROMACS package with cubic periodic boundary conditions.[4] The equations for the motion of all atoms were integrated using a classic Verlet leapfrog integration algorithm with a time step of 1.0 fs. A cutoff radius of 1.6 nm was set for short-range van der Waals interactions and real-space electrostatic interactions. The particle-mesh Ewald (PME) summation method with an interpolation order of 5 and a Fourier grid spacing of 0.15 nm was employed to handle long-range electrostatic interactions in reciprocal space. All simulation systems were first energetically minimized using a steepest descent algorithm, and thereafter annealed gradually from 700 K to room temperature (300 K) within 10 ns. All annealed simulation systems were equilibrated in an isothermal-isobaric (NPT) ensemble for 10 ns of physical time maintained using a Nosé-Hoover thermostat and a Parrinello-Rahman barostat with time coupling constants of 0.4 and 0.2 ps, respectively, to control the temperature at 300 K and the pressure at 1 atm. Atomistic simulations were further performed in a canonical ensemble (NVT) for 20 ns, and simulation trajectories were recorded at an interval of 100 fs for further structural and dynamical analysis. Results were visualized and statistically analyzed in VMD software.
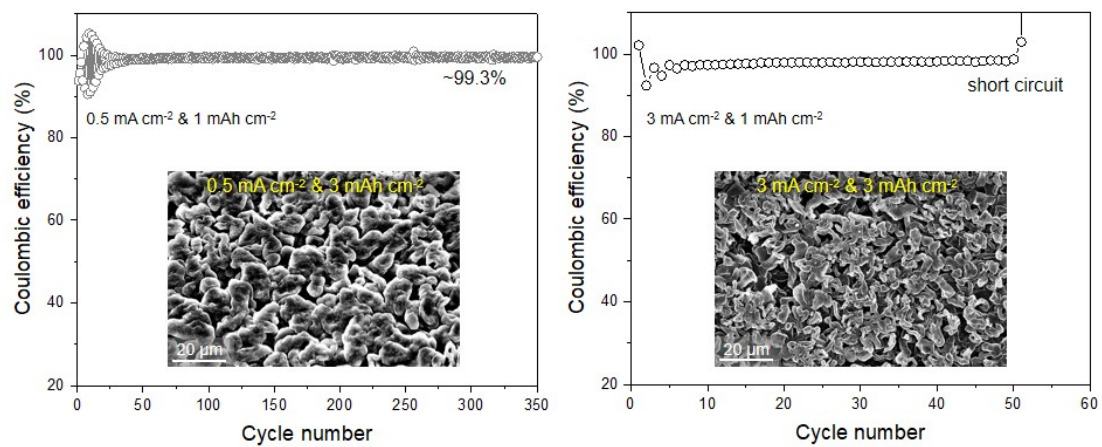
Figure S1. Cycling performance (1 mAh cm^{-2}) and Li deposition morphology (3 mAh cm^{-2}) of Li||Cu cells using Base-DEE under the current density of 0.5 mA cm^{-2} or 3 mA cm^{-2}.
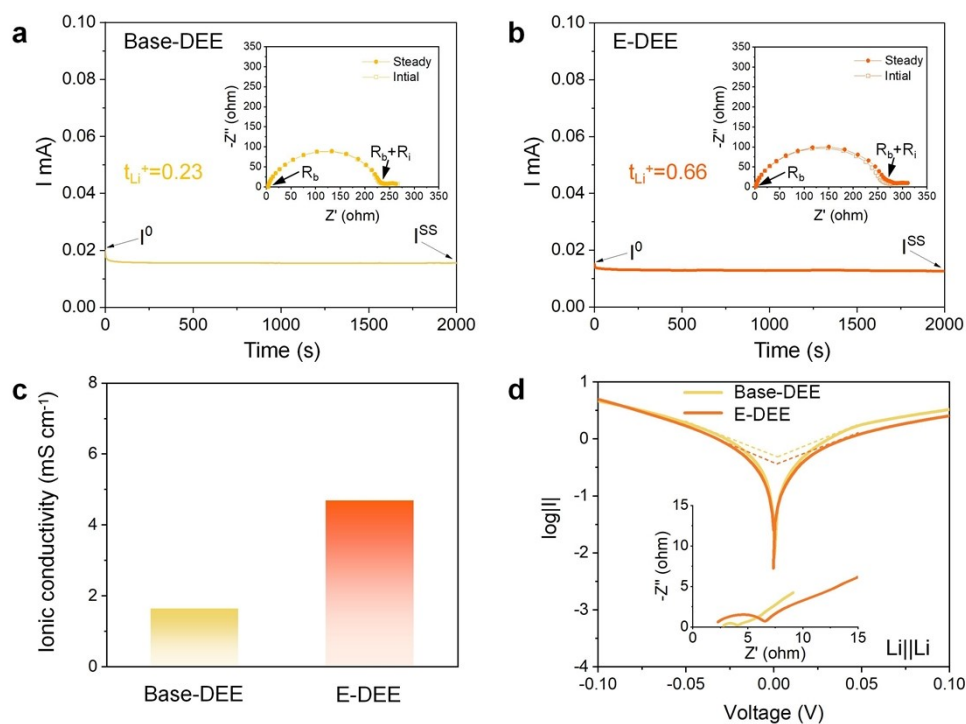
Figure S2. (a,b) Li+ transference numbers and the chronoamperometry profiles of Li||Li cells in different electrolytes. (c) Ionic conductivity and (d) exchange current density tests (inset the EIS profiles) of Base-DEE and E-DEE.
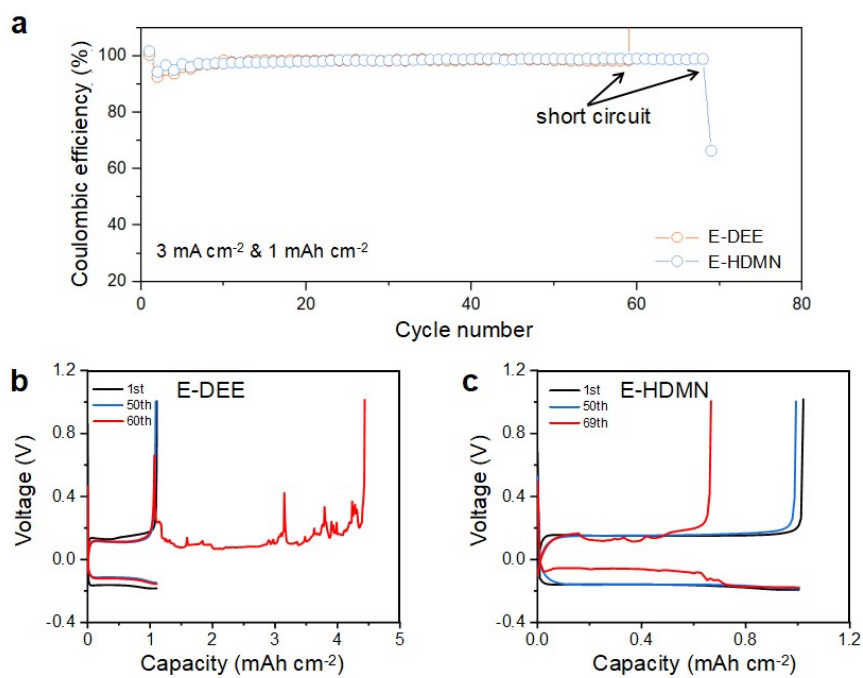
Figure S3. (a) Cycling performance of Li||Cu cells using E-DEE and E-HDMN under 3 mA cm^{-2} with 1 mAh cm^{-2} and the corresponding (b,c) voltage profiles.
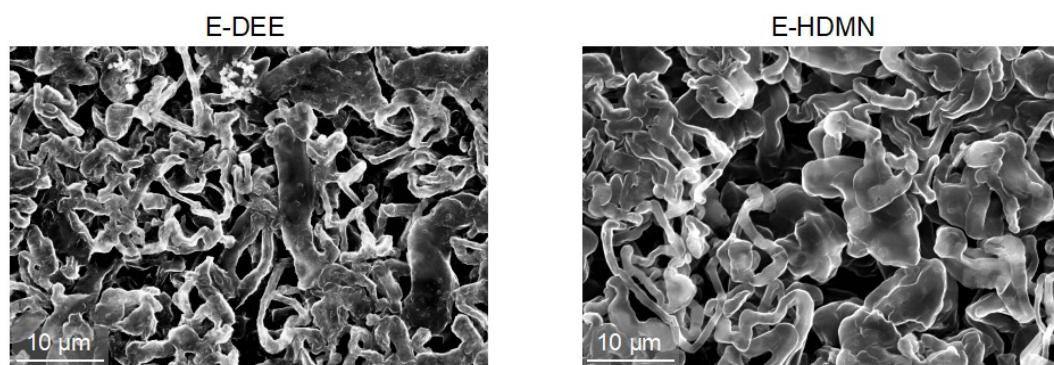
E-DEE

E-HDMN

Figure S4. SEM images of Li deposition morphology induced by E-DEE and E-HDMN under 3 mA cm^{-2} and 3 mAh cm^{-2}.

a

$E_{b\ (DEE-Li^+)} = -242.58\ \text{kJ mol}^{-1}$

b

+30 kcal mol^{-1}

-30 kcal mol^{-1}

DEE
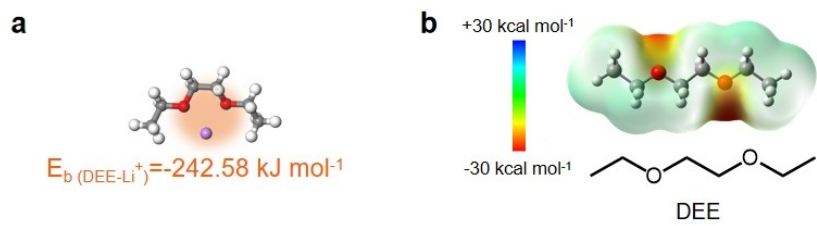
Figure S5. (a) The binding energy with Li$^+$ and (b) ESP map of DEE.
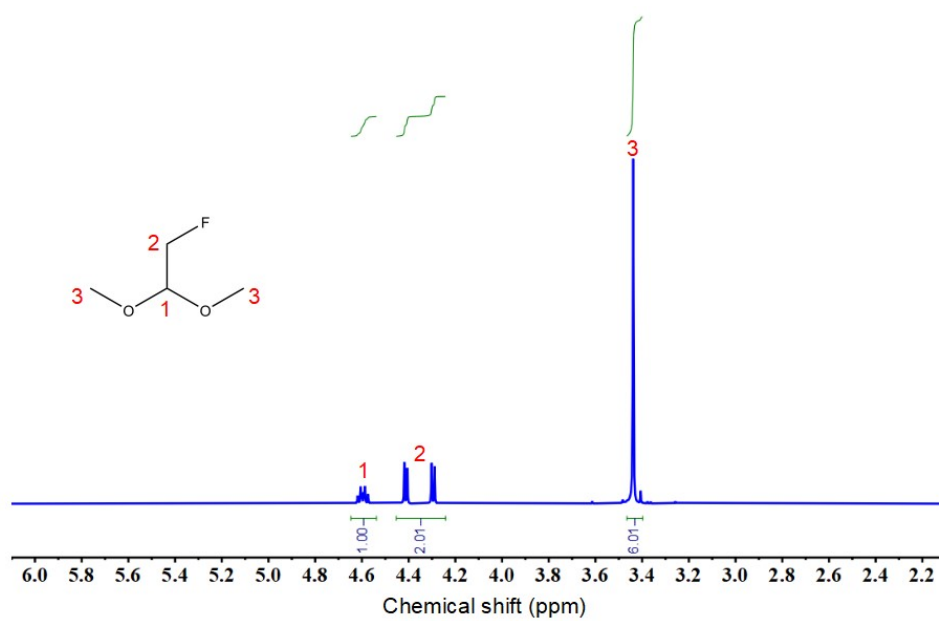
Figure S6. ^{1}H-NMR of FDMN.
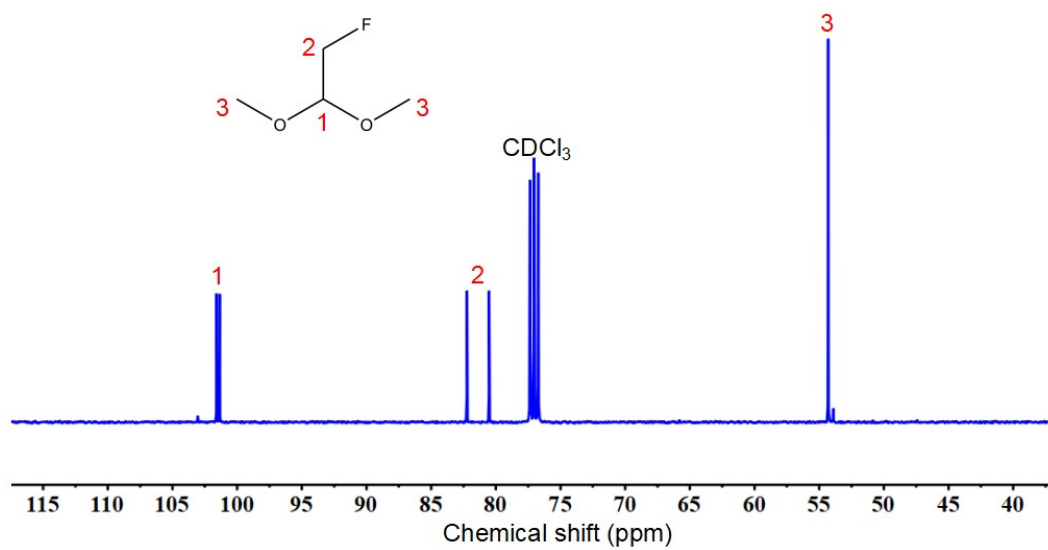
Figure S7. ^{13}C-NMR of FDMN.
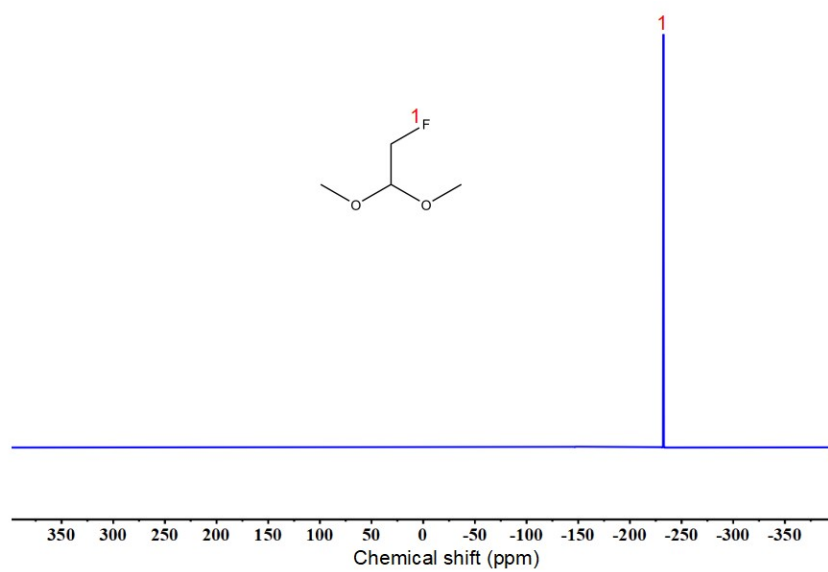
Figure S8. ^{19}F-NMR of FDMN.
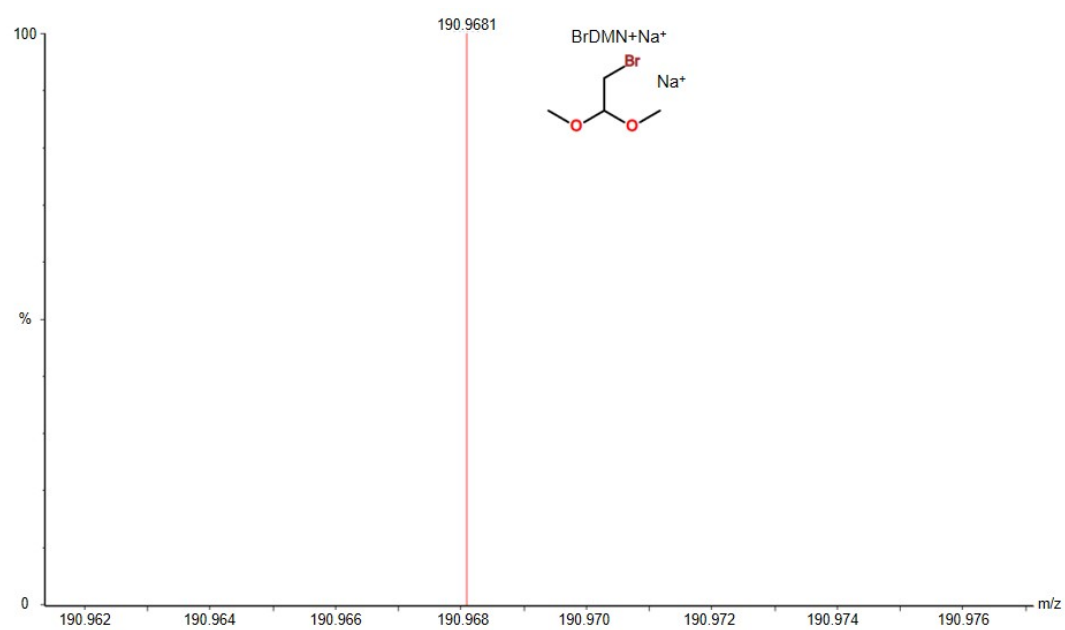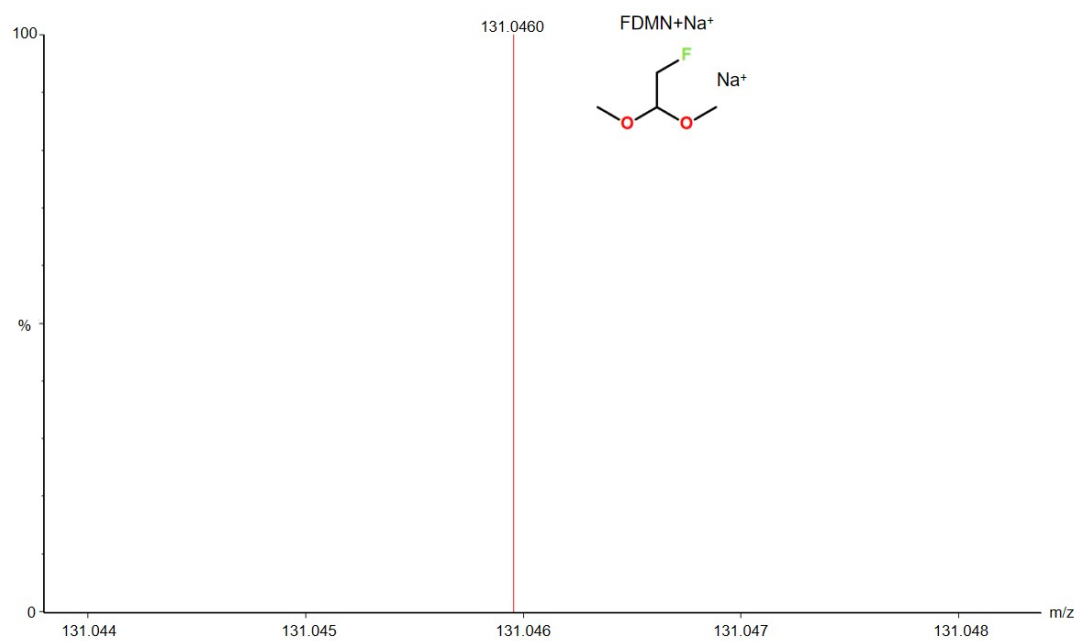
Figure S9. HPLC-TOF MS profiles of FDMN and BrDMN.
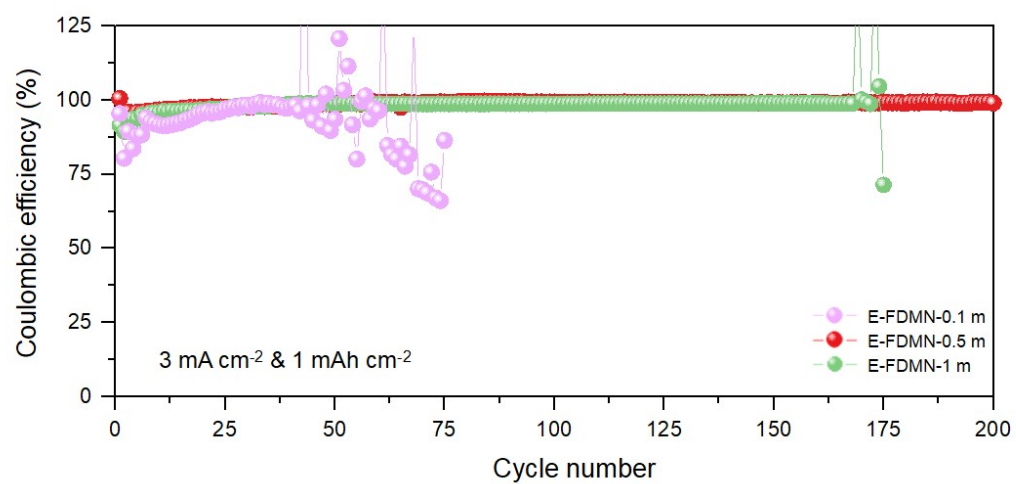
Figure S10. Cycling performance of Li||Cu cells using different FDMN addition contents of E-FDMN under 3 mA cm^{-2}.
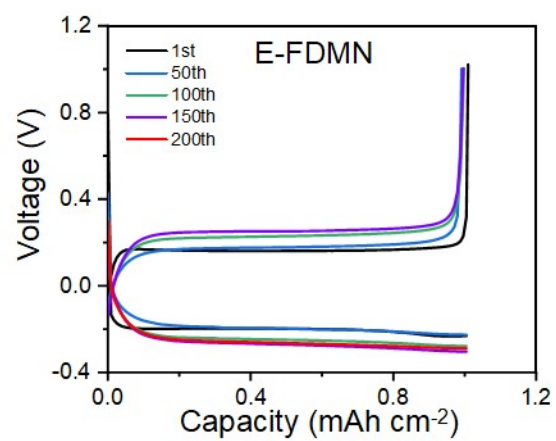
Figure S11. Voltage profiles of Li||Cu cells using E-FDMN under 3 mA cm^{-2} and 1 mAh cm^{-2}.
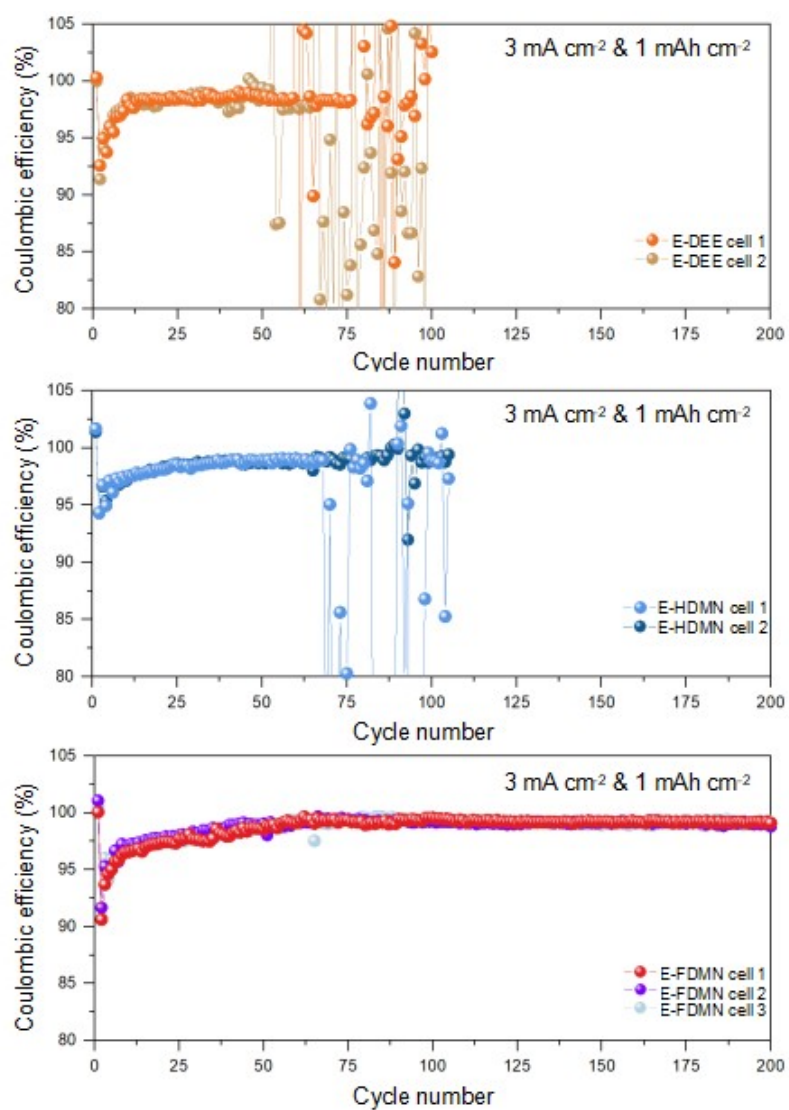
Figure S12. Repeated data of Li||Cu cells using different electrolytes under 3 mA cm^{-2} with 1 mAh cm^{-2}.
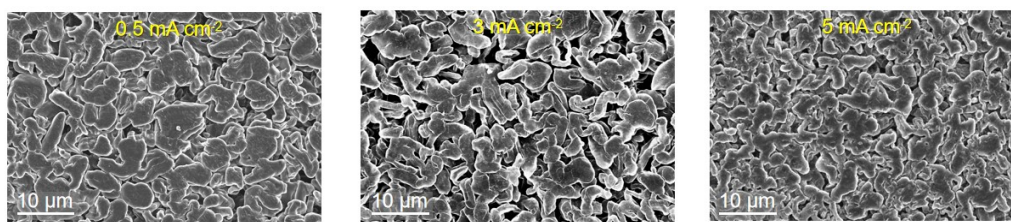
Figure S13. Li deposition morphologies on Cu at different current densities with capacity of 3 mAh cm^{-2} using E-FDMN.
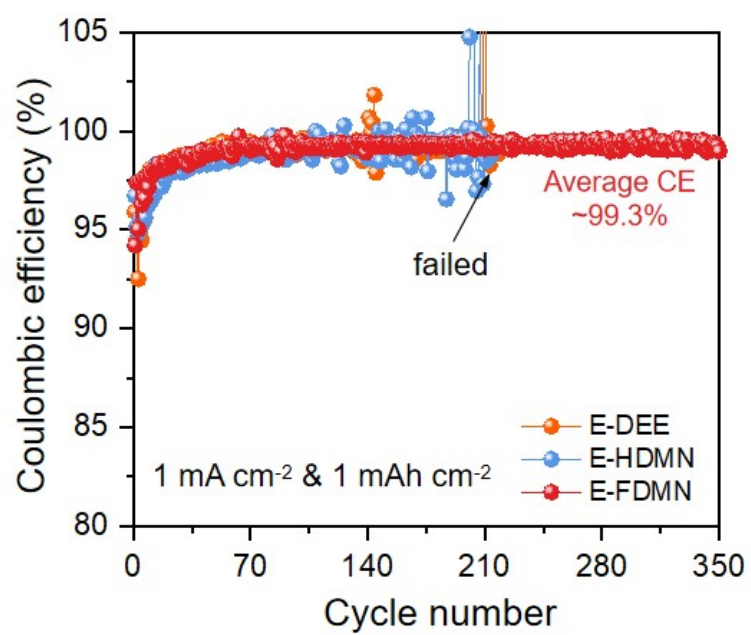
Figure S14. Cycling performance of Li||Cu cells using different electrolytes under 1 mA cm^{-2} with 1 mAh cm^{-2}.
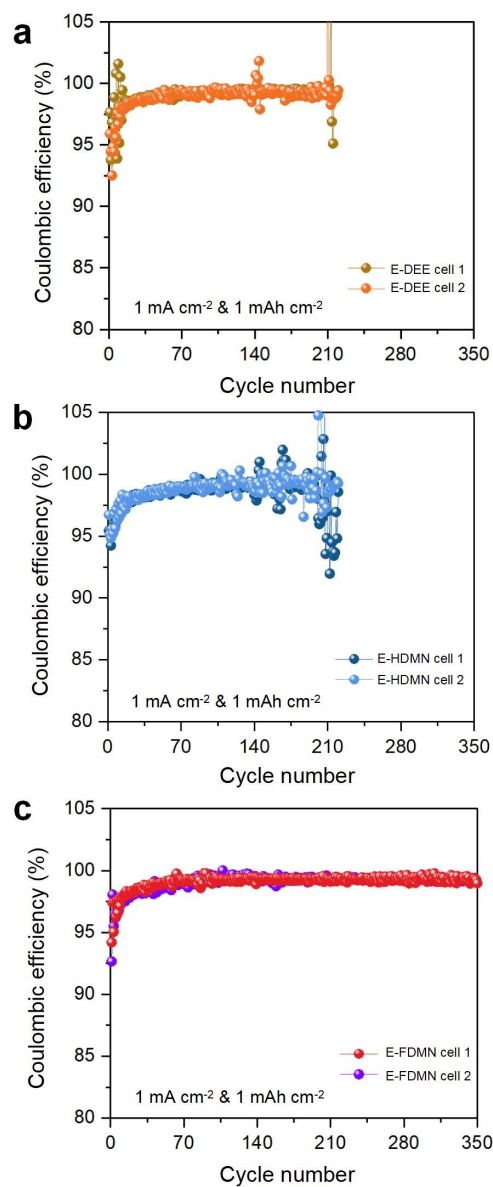
Figure S15. Repeated data of Li||Cu cells using (a) E-DEE, (b) E-HDMN and (c) E-FDMN under 1 mA cm^{-2} with 1 mAh cm^{-2}.
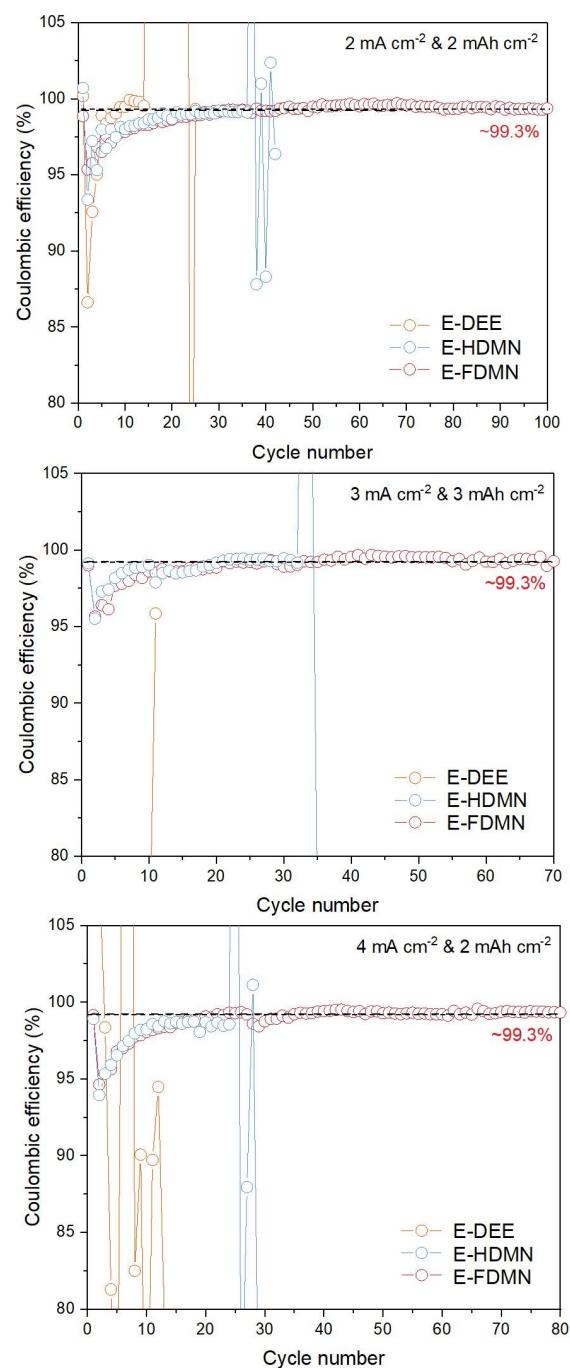
Figure S16. Cycling performance of Li||Cu cells using different electrolytes under different current densities and capacities.
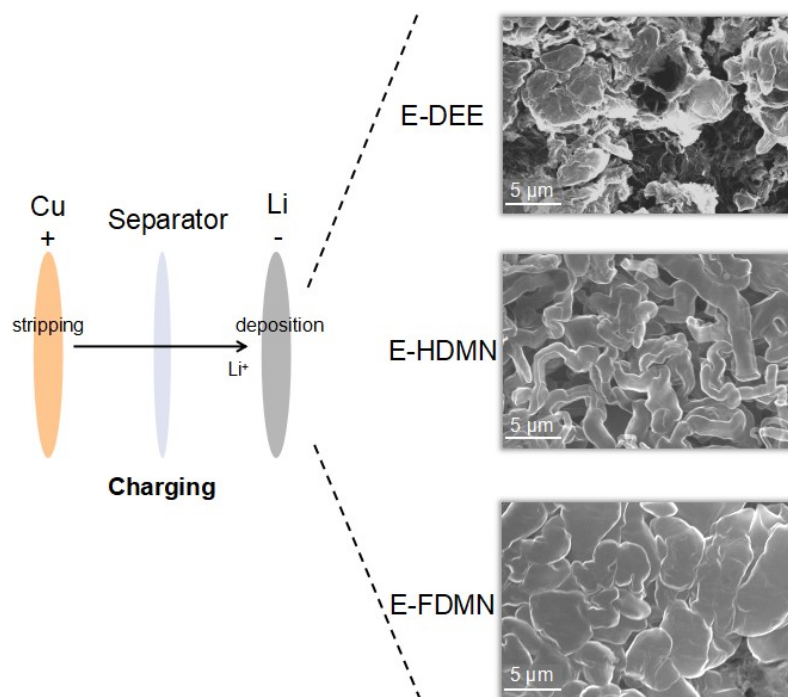
Figure S17. Li deposition on the Li side of Li||Cu cells using different electrolytes after 50 cycles under 3 mA cm^{-2} with a capacity of 1 mAh cm^{-2}.
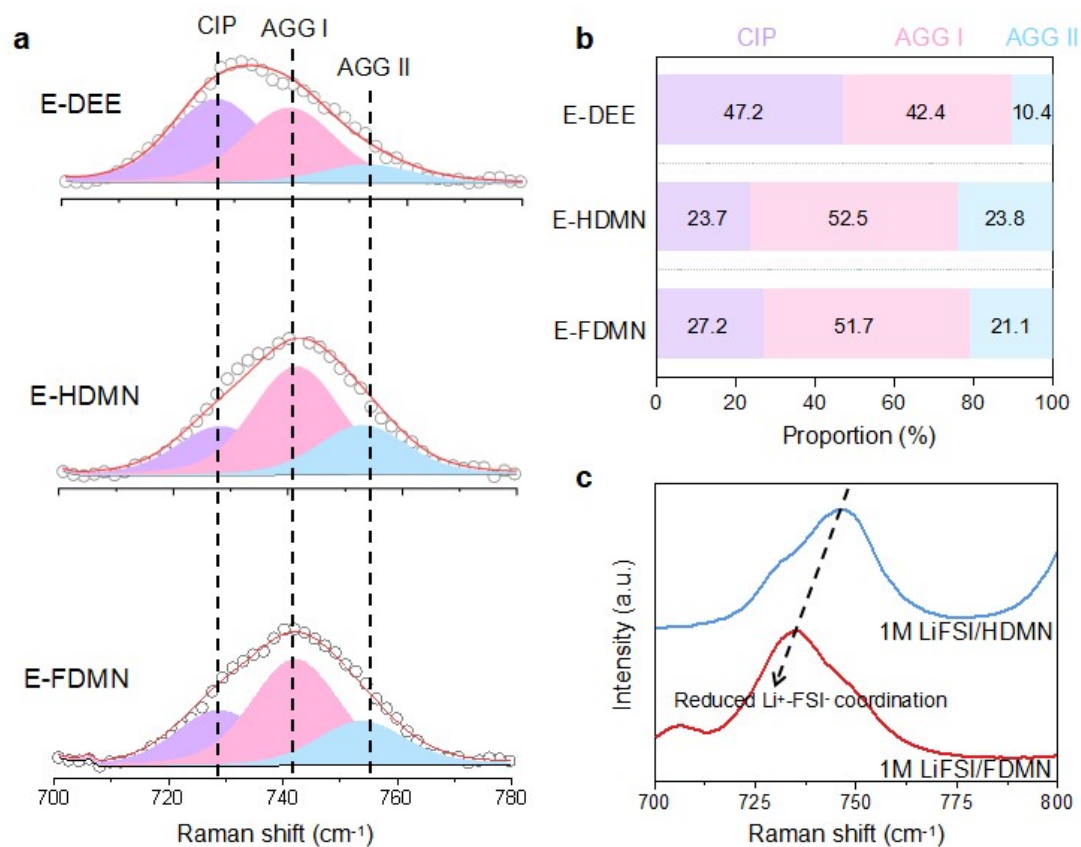
Figure S18. (a) Raman spectra and the corresponding peak proportions of the three electrolytes. (c) Raman spectra of dilute electrolytes using HDMN and FDMN solvents.
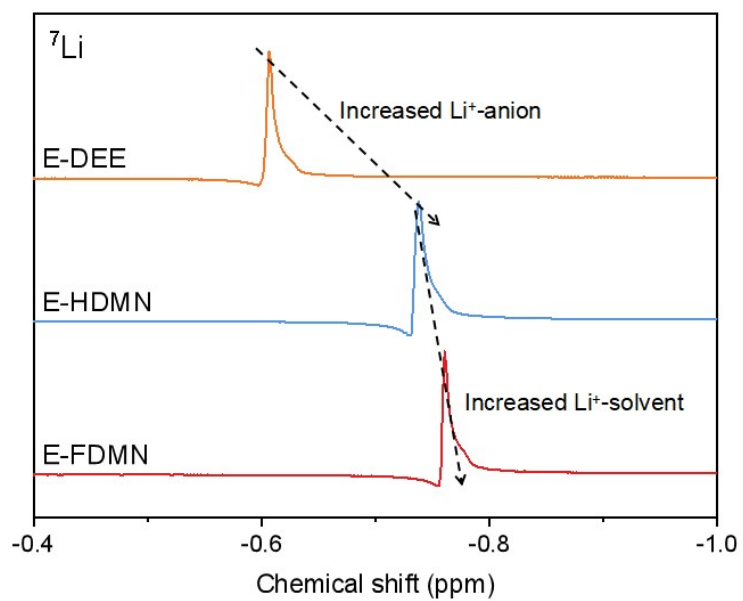
Figure S19. ^{7}Li-NMR of different electrolytes.
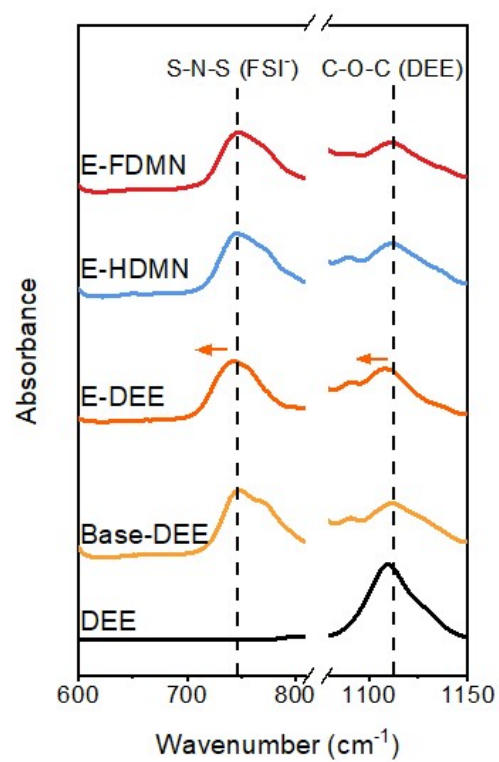
Figure S20. FT-IR spectra of different electrolytes.
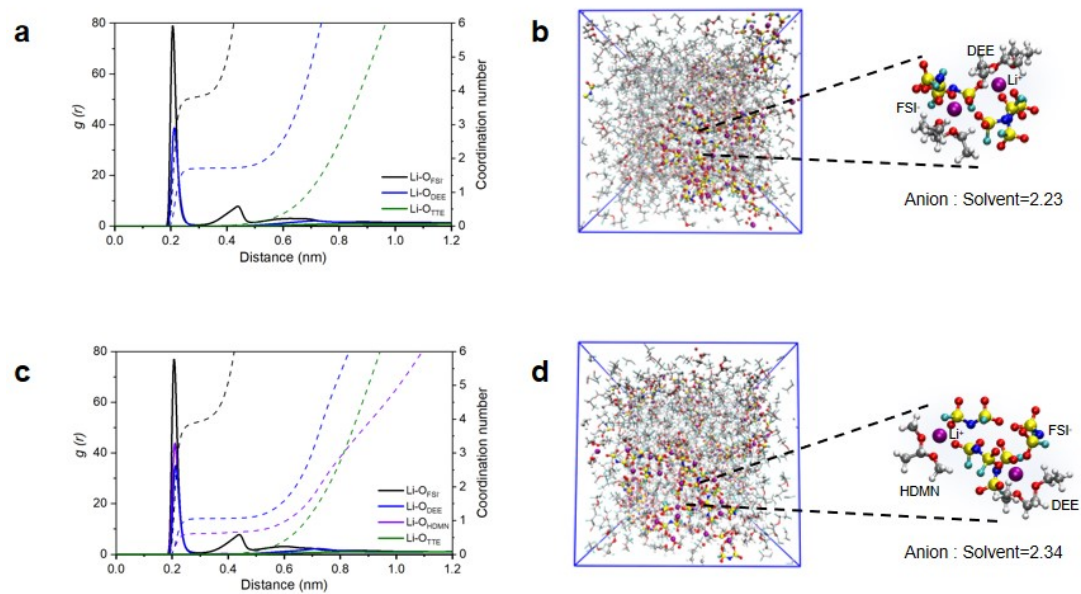
Figure S21. RDF, coordination number and solvation structure snapshot from the MD simulation of (a,b) E-DEE and (c,d) E-HDMN.
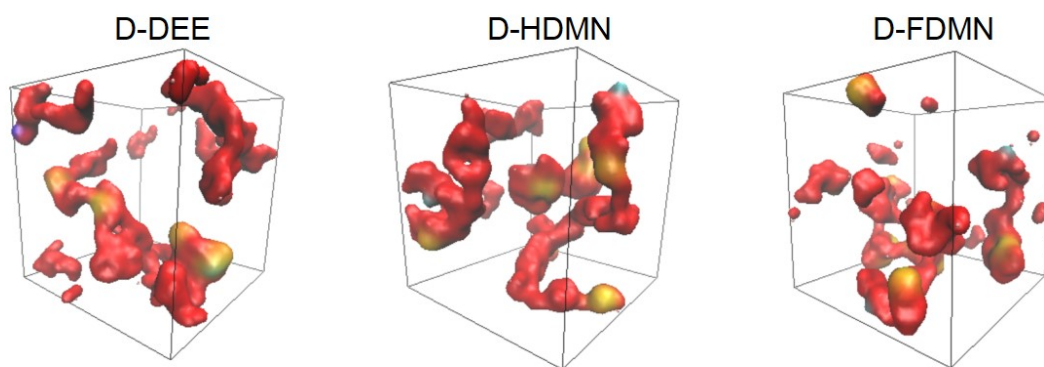
Figure S22. Snapshots of Li^+-FSI^- clusters in different electrolytes from the MD simulation.
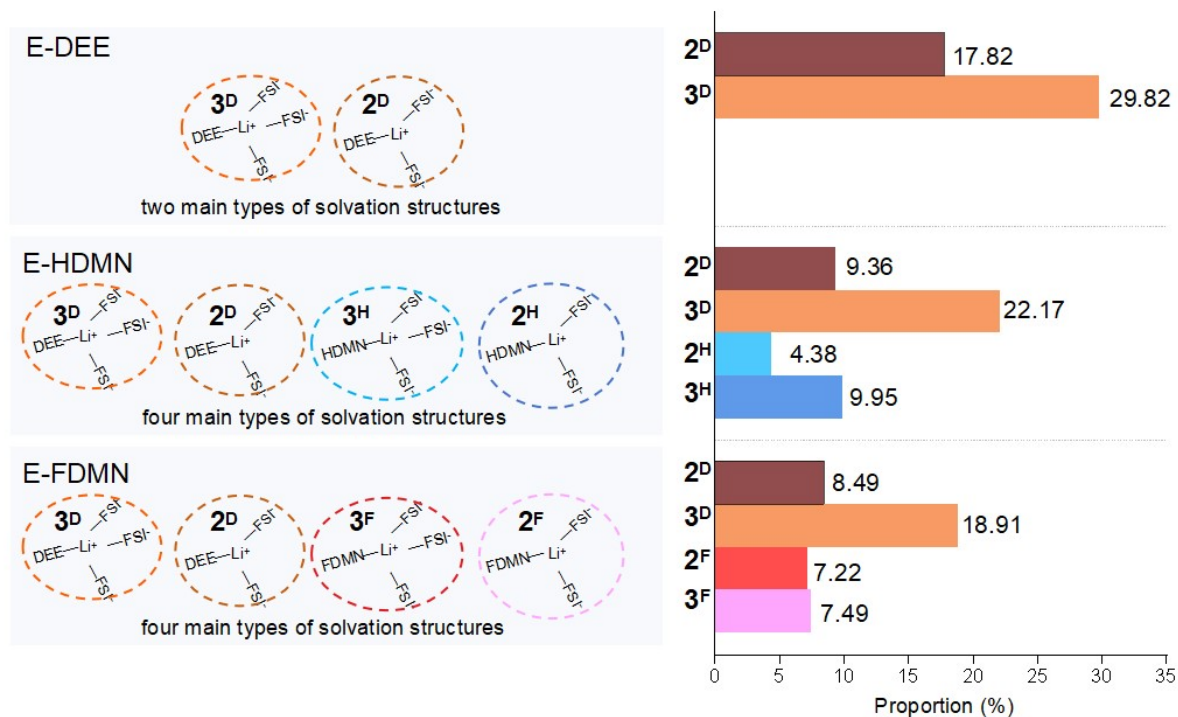
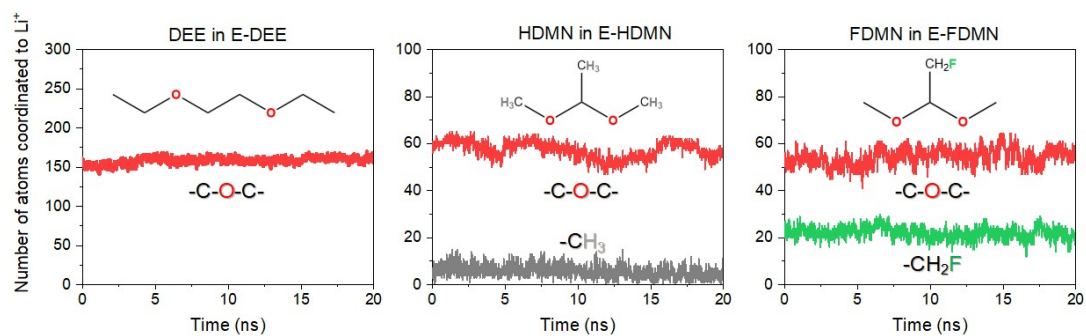**Figure S23.** Statistical ratios of the main solvation structures for different electrolytes from MD simulations.

Figure S24. Statistics on the number of corresponding atoms of different molecules with a distance of 3 Å to Li⁺ (the inner solvation layer) from the MD simulations.
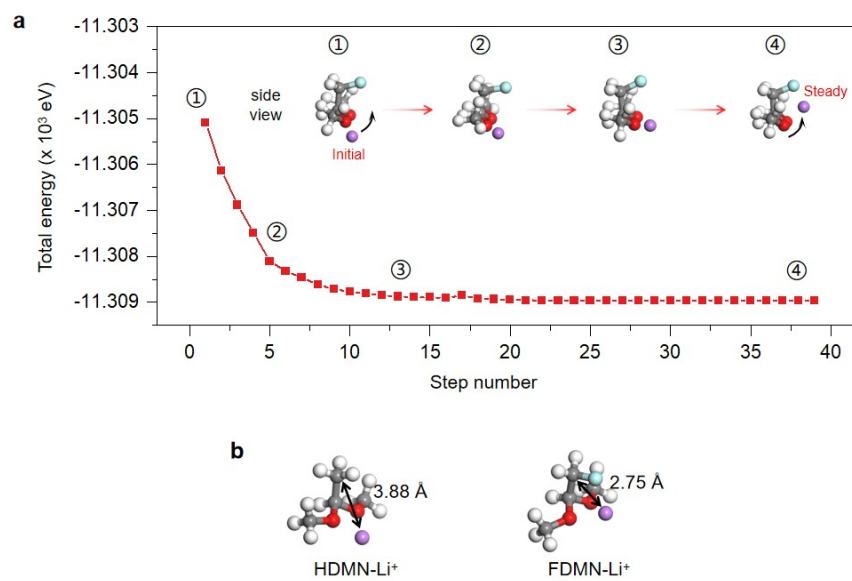
Figure S25. (a) Total energy change curves of FDMN-Li+ structure optimization process. (b) Stable structures of HDMN-Li+ and FDMN-Li+.
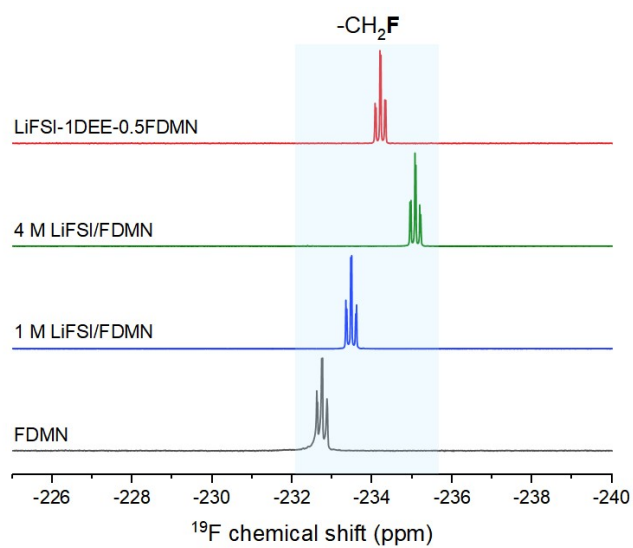
Figure S26. ^{19}F-NMR spectra of the -CH$_2$F in FDMN of different electrolytes.

Note: ^{19}F-NMR was performed to detect the interaction between the F atom in FDMN and Li$^+$. The chemical shift of -CH$_2$F moves to a higher field with the addition of LiFSI in FDMN. A similar change was observed when FDMN was used as a co-solvent in the high concentration electrolyte (LiFSI-1DEE-0.5FDMN).
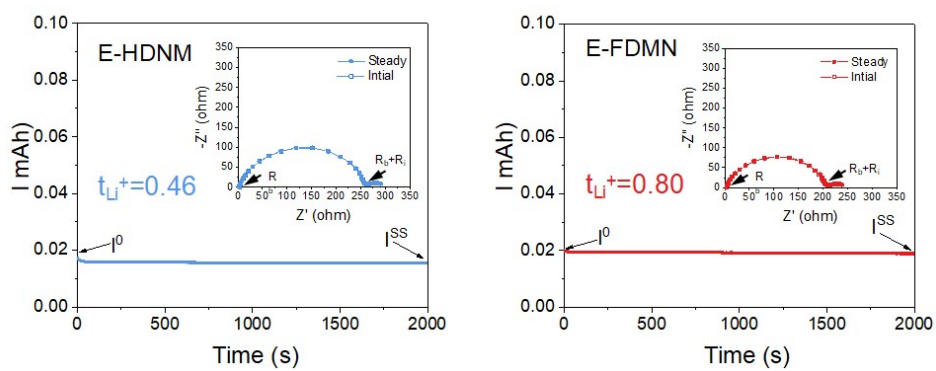
Figure S27. Li$^+$ transference numbers and the chronoamperometry profiles of Li||Li cells in different electrolytes.
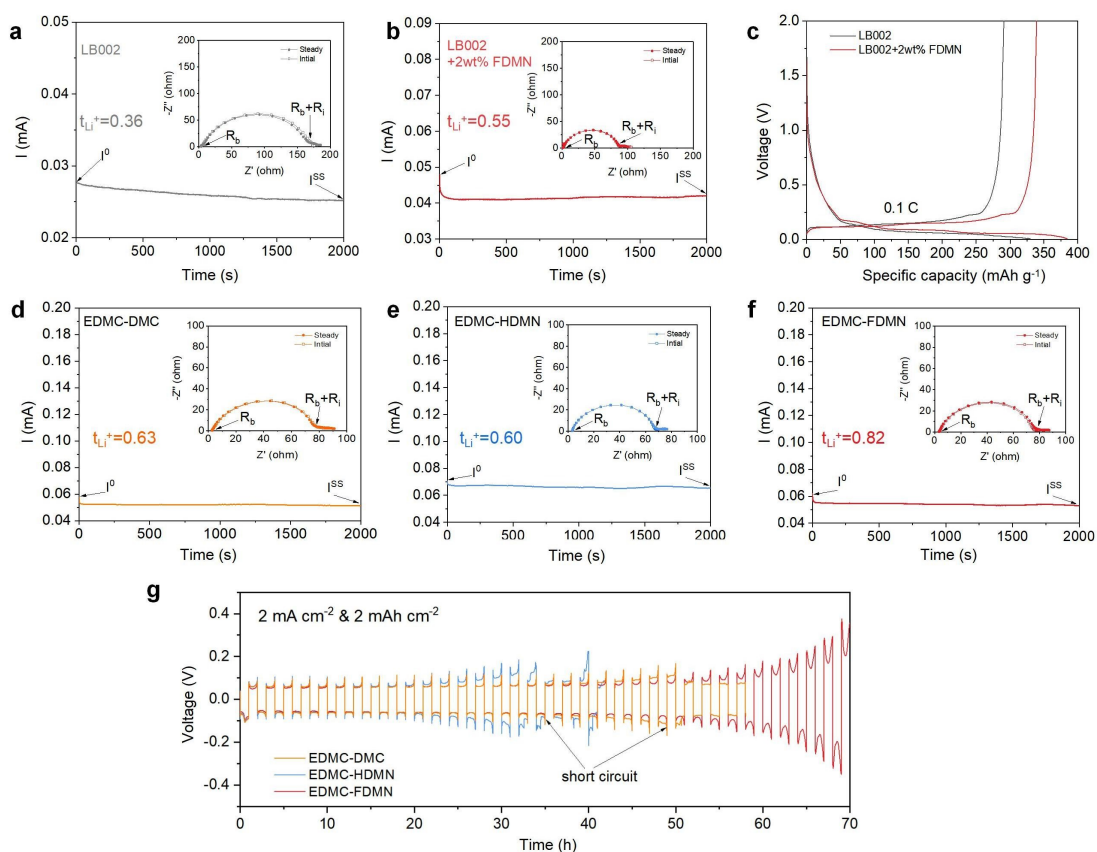
Figure S28. Li⁺ transference number tests using LB002 (a) without and (b) with FDMN and the corresponding initial charge/discharge curves of Li||Graphite cells. (d-f) Li⁺ transference number tests in different ester-based LHCEs and (g) cycling performance of Li||Li cells.
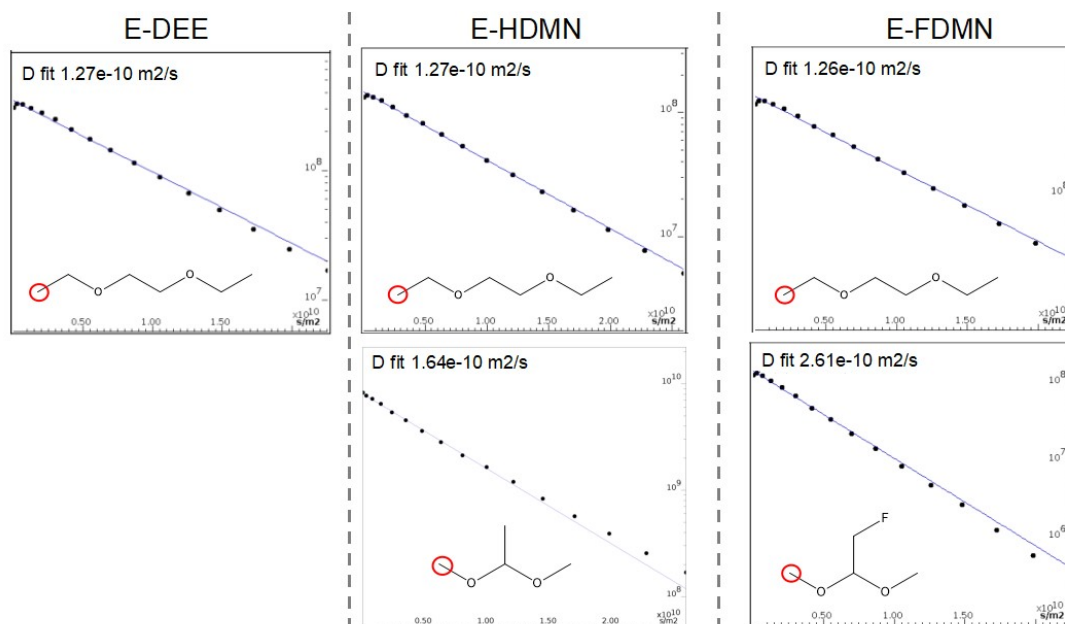
Figure S29. Curve fitting of self-diffusion coefficient for solvents in different electrolytes.
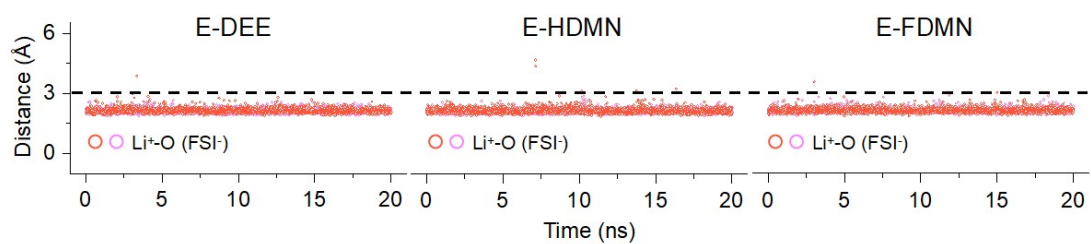
Figure S30. The evolvement of the distance between Li$^+$ and nearby atoms of FSI$^-$ in the solvation structure of different electrolytes from molecular dynamics simulations (select one FSI$^-$ anion as a representative).
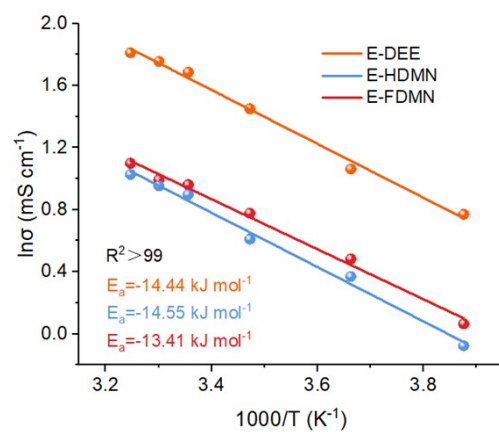
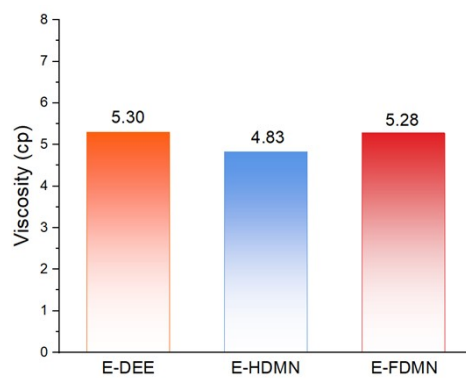**Figure S31.** Ion conduction activation energy of different electrolytes.
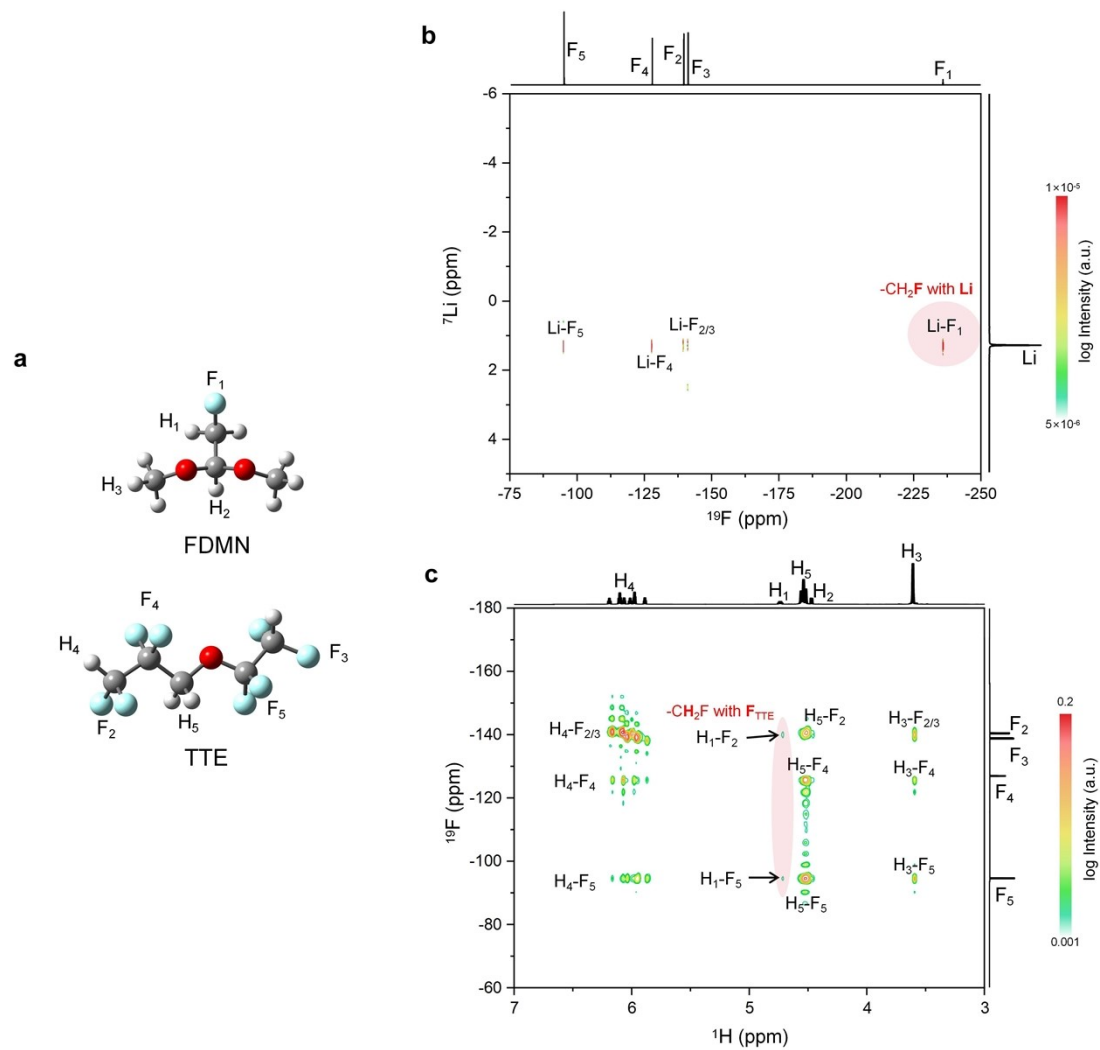
Figure S32. Viscosity test of different electrolytes.

Figure S33. (a) Schematic illustration of different atoms in FDMN and TTE. (b) 2D ^{7}Li-^{19}F NMR of E-FDMN and (b) 2D ^{1}H-^{19}F NMR of FDMN-TTE mixture (1: 6 in mole ratio).
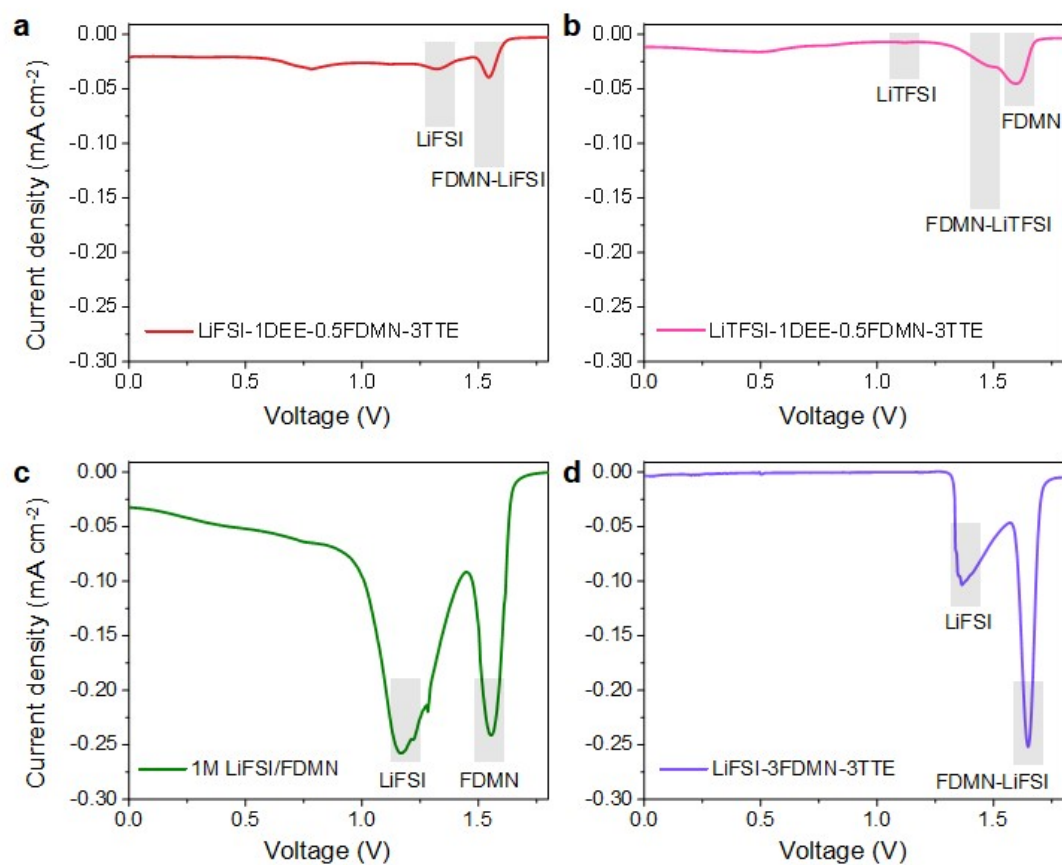
Figure S34. LSV of the Li||Cu cells using different FDMN-based electrolytes.
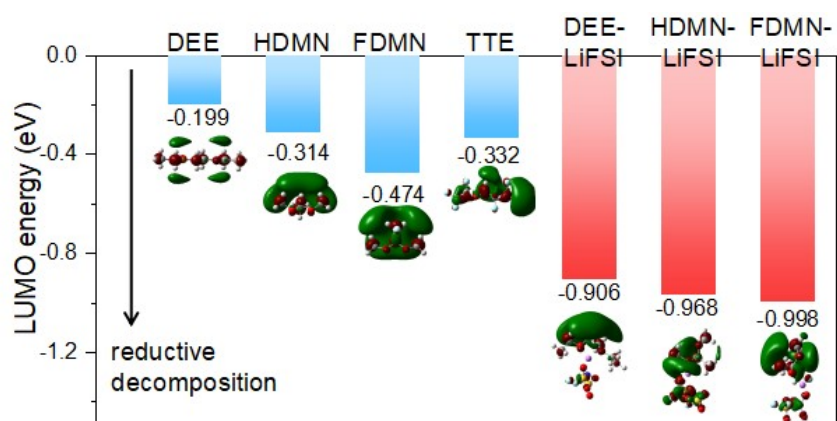
Figure S35. Calculated LUMO energy of the different solvents, diluent and solvent/salt complexes.

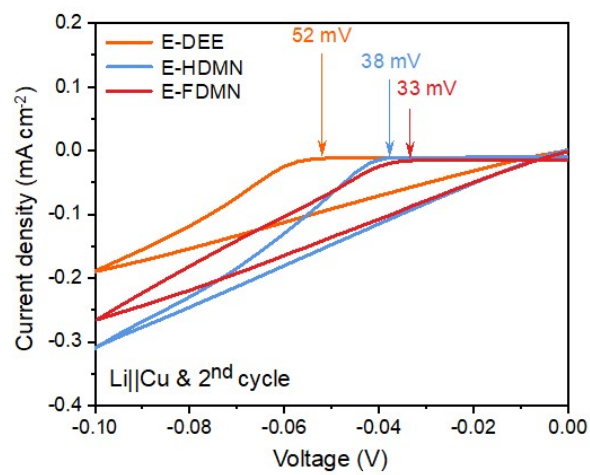**Figure S36.** The 2nd CV cycle of Li||Cu cells in different electrolytes.
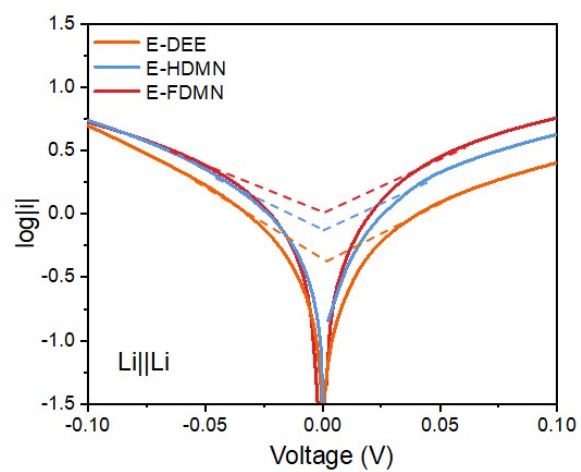
Figure S37. Exchange current density measurements of SEIs formed by different electrolytes.
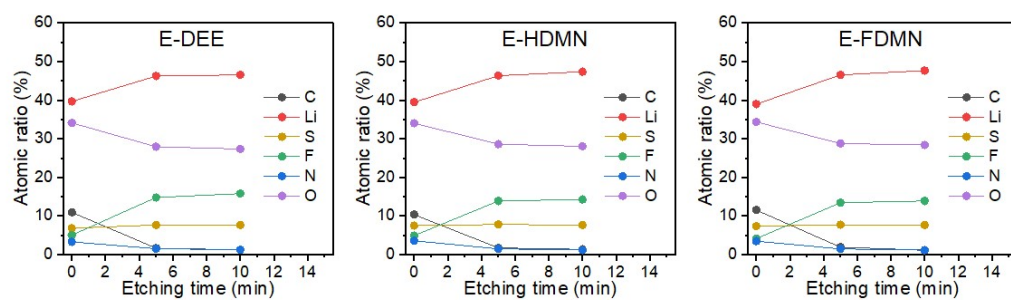
Figure S38. Atomic distribution ratios obtained from XPS depth profiles of Li||Cu cell cycled in different electrolytes.
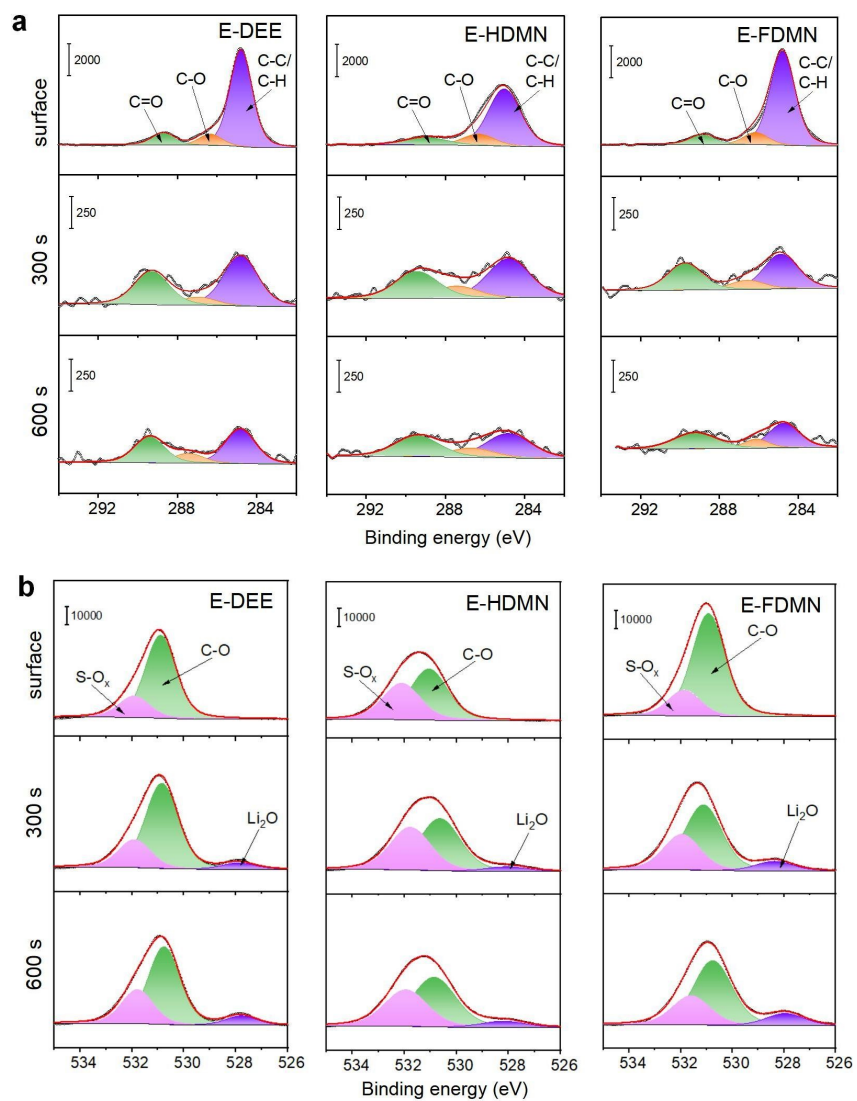
Figure S39. (a) C 1s and (b) O 1s spectra obtained from XPS depth profiles of Li||Cu cells cycled in different electrolytes.
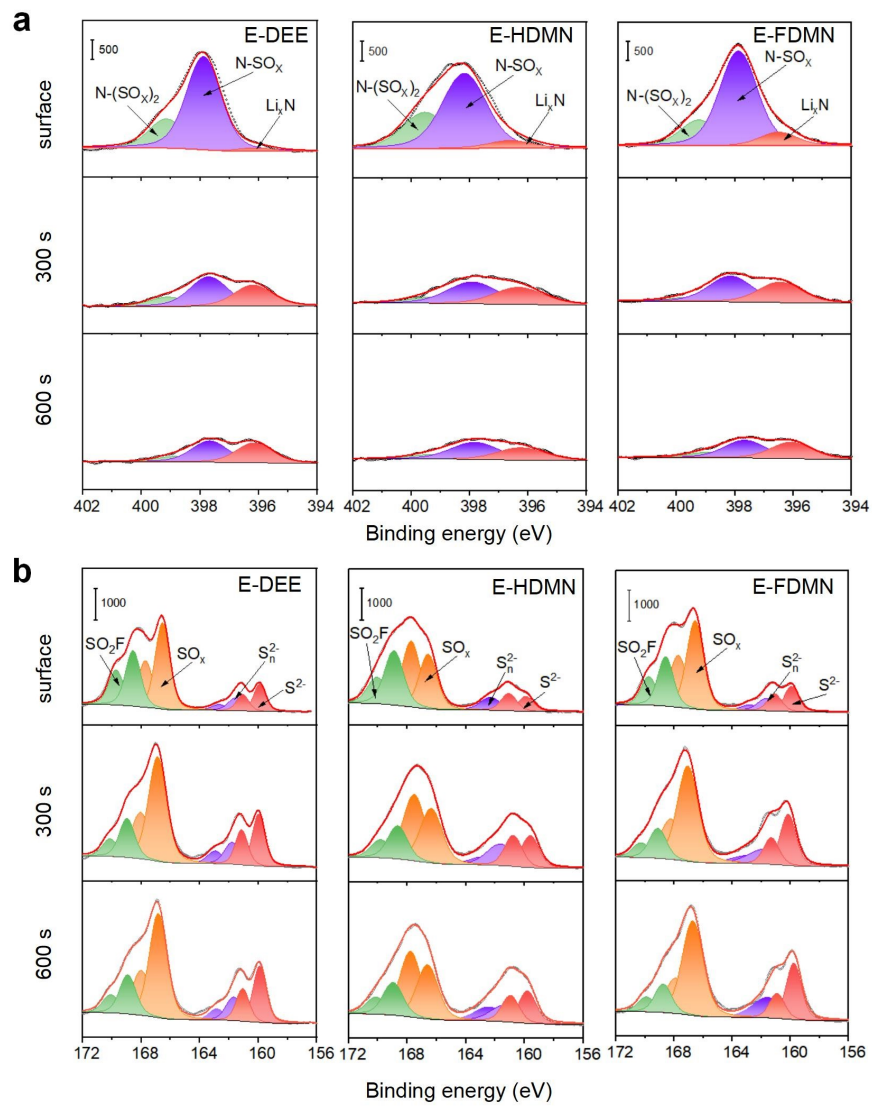
Figure S40. (a) N 1s and (b) S 2p spectra obtained from XPS depth profiles of Li||Cu cells cycled in different electrolytes.
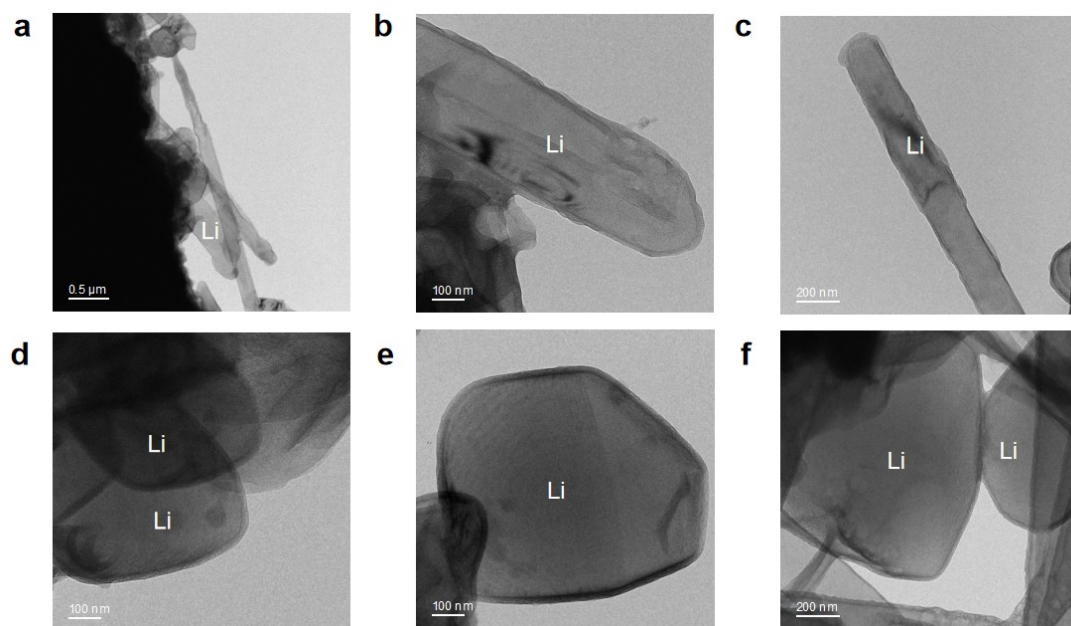
Figure S41. Cryo-TEM images of deposited Li on Cu TEM grid using (a-c) E-DEE and (d-f) E-FDMN under 3 mA cm^{-2}.
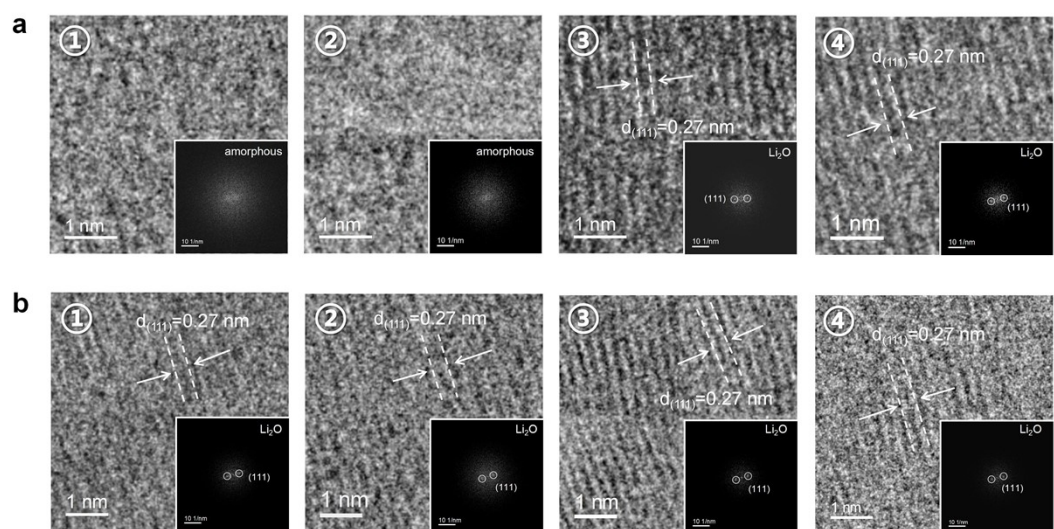
Figure S42. HR-TEM and corresponding FFT images of (a) E-DEE and (b) E-FDMN derived SEIs in different regions of Figure 4f, j.
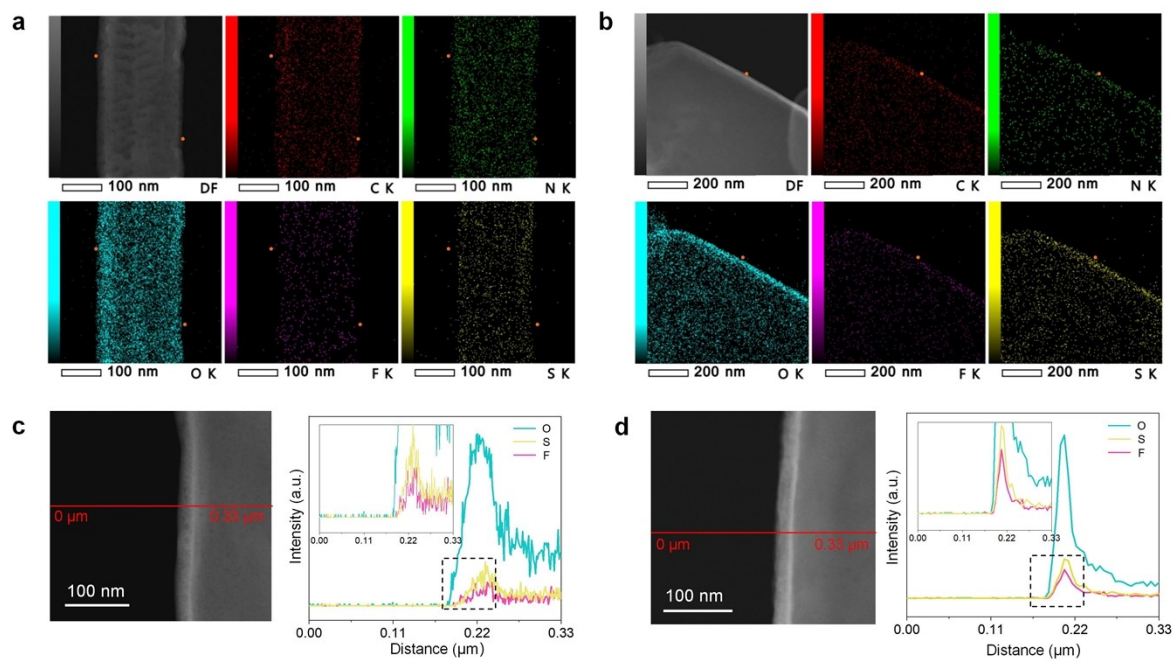
Figure S43. EDS map (orange dots mark the SEI boundary) and line scans of the SEIs formed by (a,c) E-DEE and (b,d) E-FDMN.
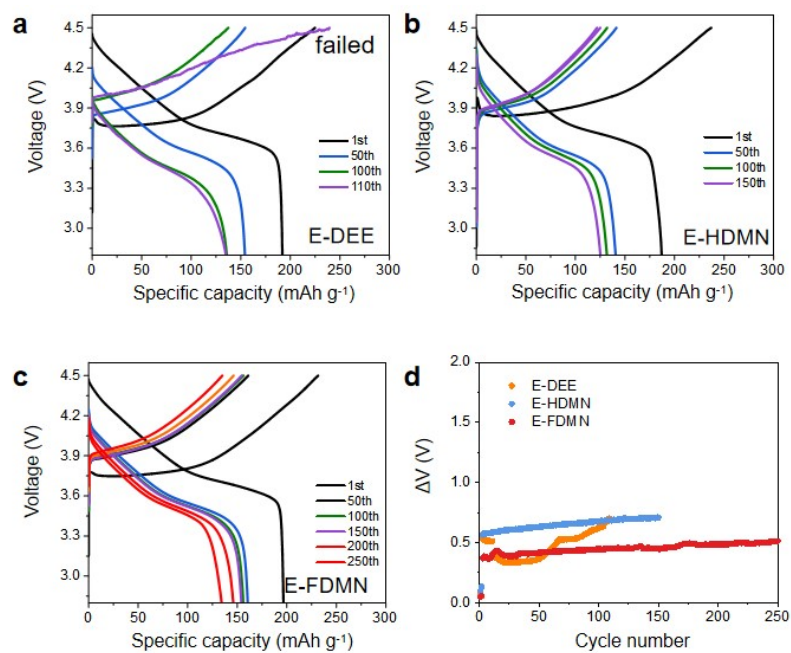
Figure S44. (a-c) Voltage profiles of NMC622||Li cells using different electrolytes under 1 C and (d) the corresponding overpotential ΔV curves.

Note: The polarization of the cell with E-FDMN is significantly lower that of E-HDMN, while the ΔV growth of the cell using E-DEE due to the interfacial deterioration during cycling.
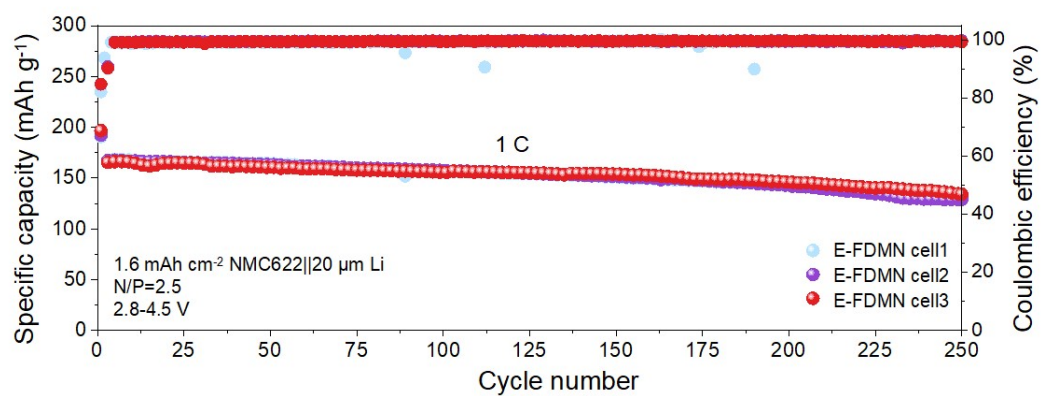
Figure S45. Repeated data of NMC622||Li cells using E-FDMN at 1C.
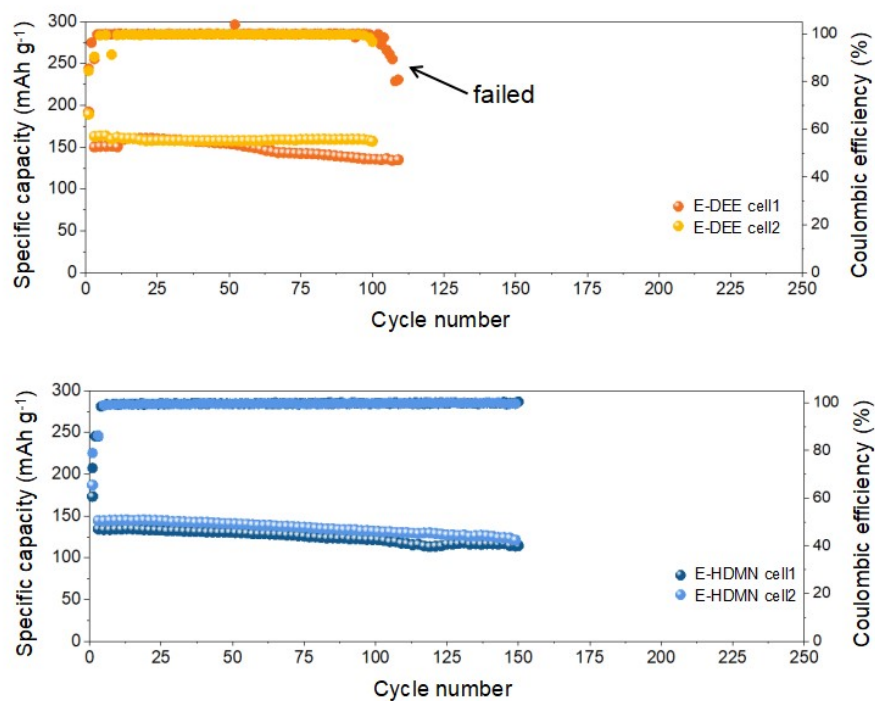
Figure S46. Repeated data of NMC622||Li cells using E-DEE and E-HDMN at 1 C.
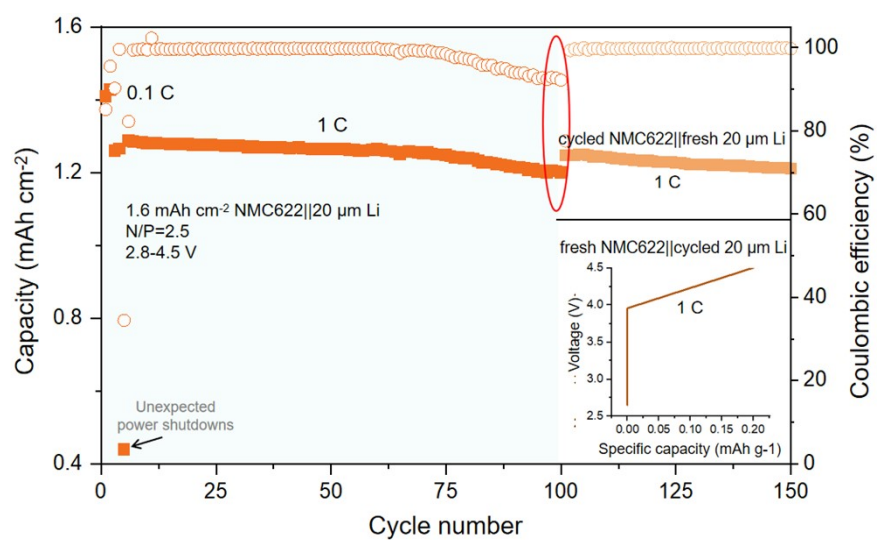
Figure S47. The performance of the cells reassembled with fresh NMC622 cathode or Li anode after the E-DEE cell failure.
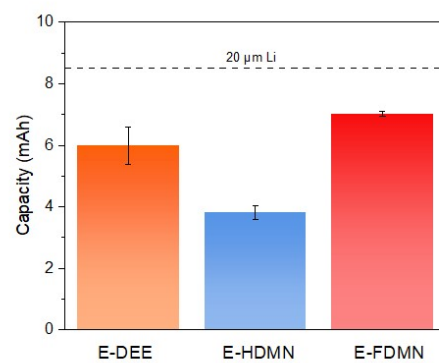
Figure S48. The quantification of active Li of cycled NMC||Li cells with different electrolytes after 100 cycles at 1 C.
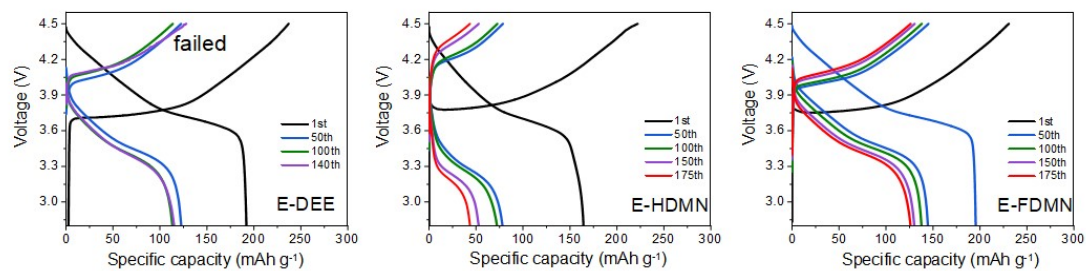
Figure S49. Voltage profiles of NMC622||Li cells using different electrolytes under 2 C.
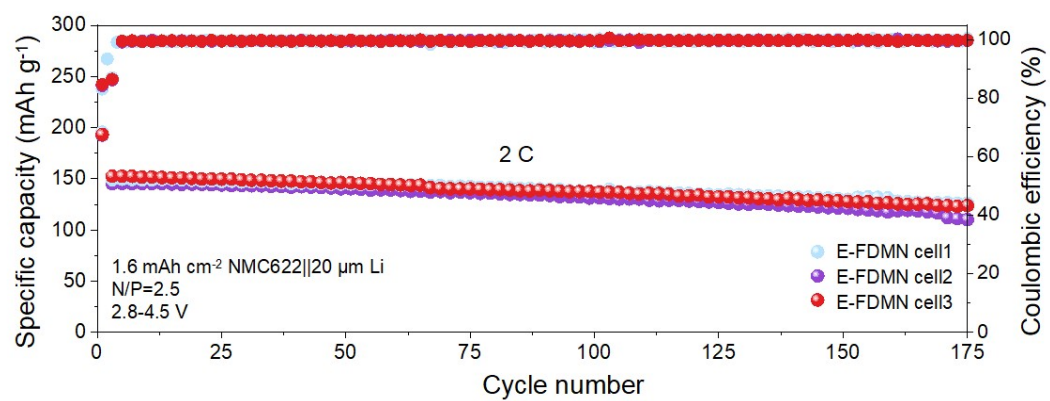
Figure S50. Repeated data of NMC622||Li cells using E-FDMN at 2 C.
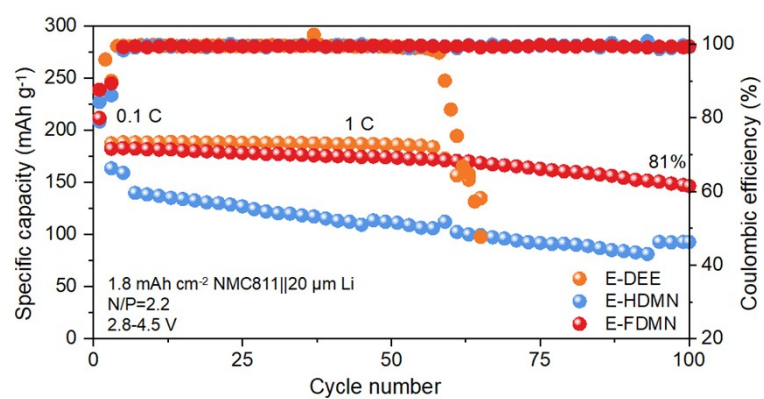
Figure S51. Cycling performance of NMC811||Li with N/P=2.2 at 1 C using different electrolytes.
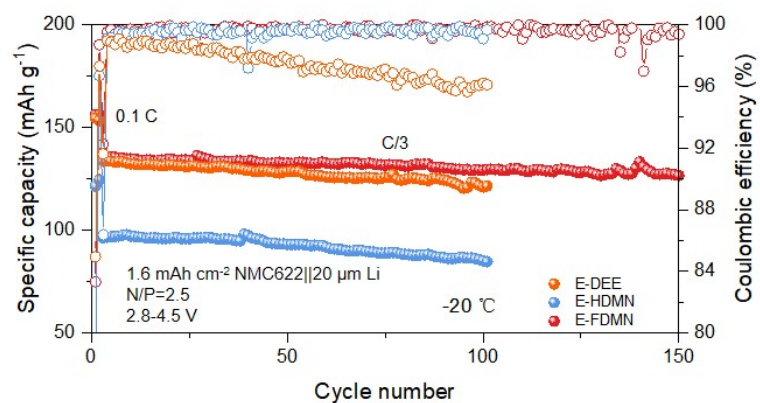
Figure S52. Cycling performance of NMC622||Li cells using three electrolytes at -20 °C.

Note: NMC622||Li cell with E-FDMN exhibits stable C/3 charging and discharging performance at -20 °C under high-voltage and low N/P ratio, while that using E-DEE shows decreased CE during cycling resulting in uncontrolled Li deposition/stripping at low-temperature. Moreover, the cell in E-FDMN also releases higher capacity compared to the weakly solvated electrolyte E-HDMN.
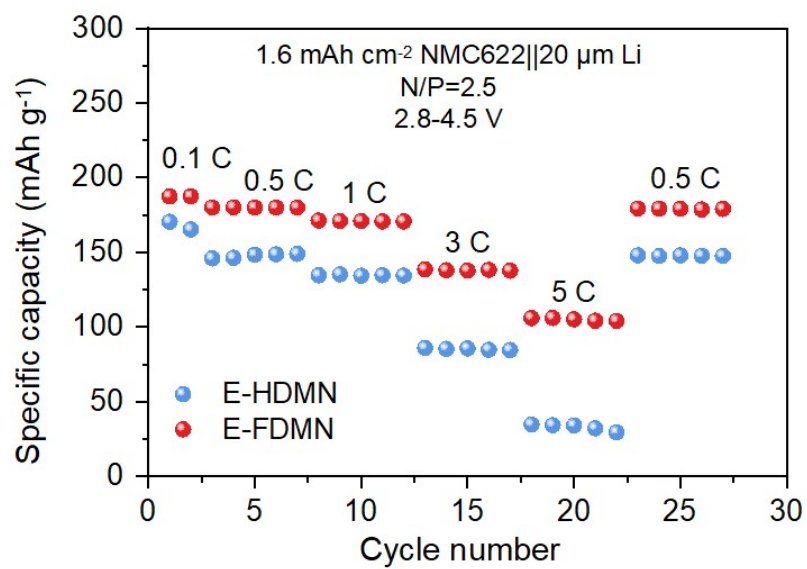
Figure S53. Rate performance of NMC8622||Li cells using different electrolytes.

Figure S54. Comparison of high-voltage and fast-charging capability of different electrolytes applied in the full cells of NMC-based cathode with thin Li anode (Details are shown in Table S3).
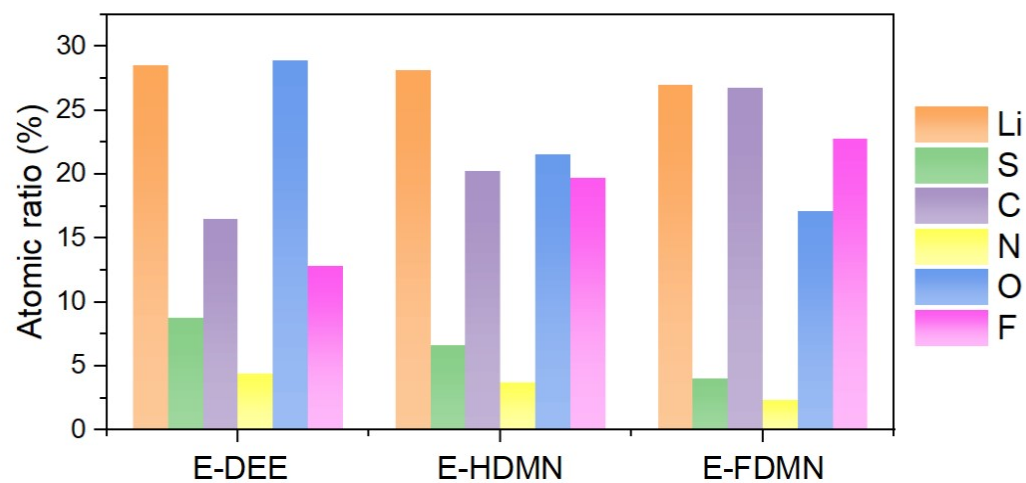
Figure S55. Atomic distribution ratios obtained from XPS of the cycled cathodes from NMC622||Li cells in different electrolytes.
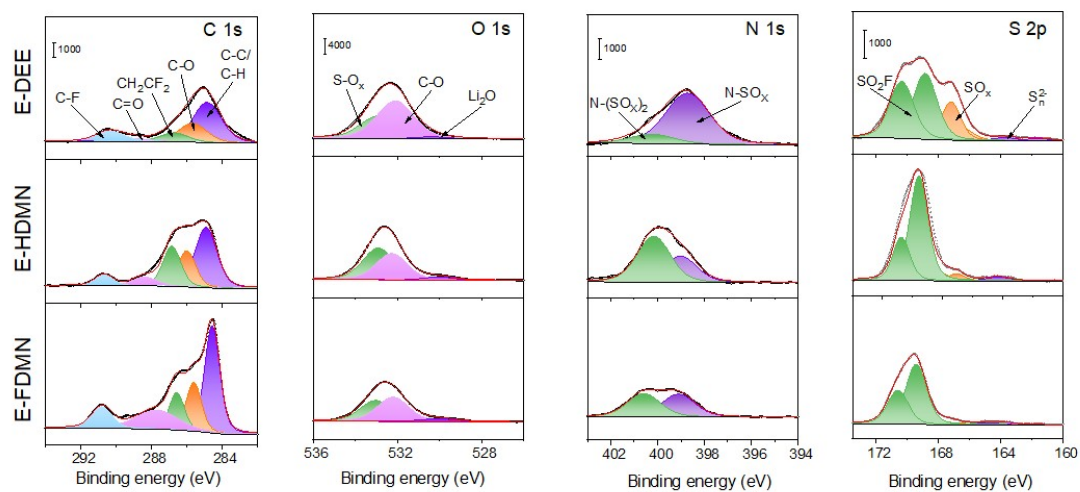
Figure S56. C 1s and O 1s spectra obtained from XPS of the cycled cathodes from NMC622||Li cells in different electrolytes.
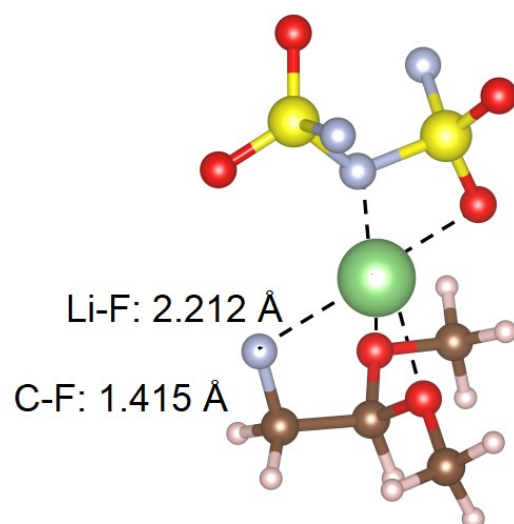
Figure S57. Optimized structure of solvation structure in E-FDMN in the absence of NiO surface.
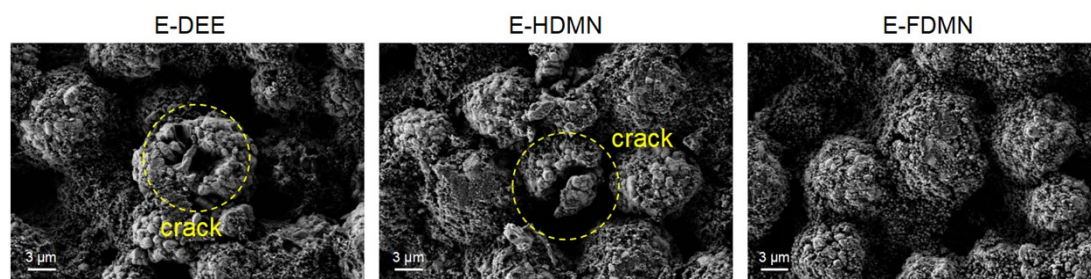
Figure S58. SEM images of the pristine and cycled NMC622 from NMC622||Li cells using different electrolytes.
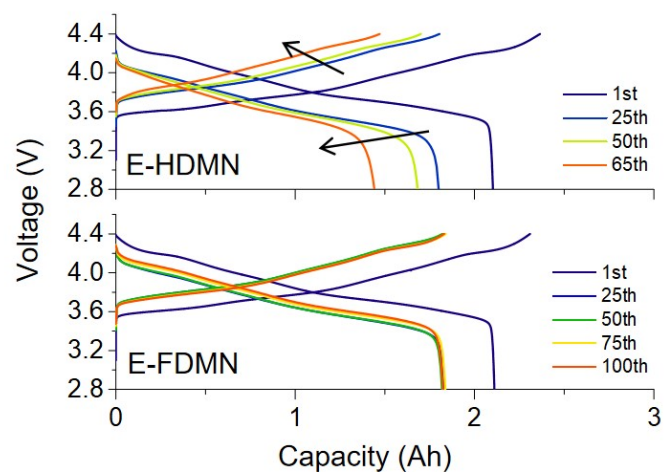
Figure S59. Charge-discharge curves of pouch cells using different electrolytes.

Table S1. Comparison of the rapid Li deposition on Li||Cu cells with different electrolytes.

Electrolytes	Current density & Capacity	Li CE	Reference
LiFSI-1DEE-0.5FDMN-3TTE	3 mA cm^{-2} & 1 mAh cm^{-2}	99.20%	This work
	2 mA cm^{-2} & 2 mAh cm^{-2}	99.30%	
	3 mA cm^{-2} & 3 mAh cm^{-2}	99.30%	
	4 mA cm^{-2} & 2 mAh cm^{-2}	99.30%	
2 M LiFSI-3BTFM-1DME	2 mA cm^{-2} & 3 mAh cm^{-2}	99.30%	[1]
1.2 M LiFSI/F5DEE or 1.2 M LiFSI/F4DEE	2 mA cm^{-2} (plating), 4 mAcm^{-2} (stripping) & 4 mAh cm^{-2}	99.00%	[2]
1 M LiFSI-Me$_2$O-TFE-PFE	3 mA cm^{-2} & 3 mAh cm^{-2}	98.80%	[3]
0.3 M LiTFSI-0.3 M THF in FM:CO$_2$ (19:1)	3 mA cm^{-2} & 3 mAh cm^{-2}	98.10%	[4]
4 M LiFSI-DME	4 mA cm^{-2} & 0.5 mAh cm^{-2}	98.40%	[5]
	10 mA cm^{-2} & 0.5 mAh cm^{-2}	97.00%	
1 M LiFSI-BFE	3 mA cm-2 & 1 mAh cm-2	99.00%	[6]
	5 mA cm^{-2} & 1 mAh cm^{-2}	99.00%	
	8 mA cm^{-2} & 1 mAh cm^{-2}	99.00%	

Reference:
[1] Chem, 2023, 9, 682-697. [2] Nat. Energy, 2022, 7, 94-106. [3] Nat. Energy, 2022, 7, 548-559. [4] Joule, 2019, 3, 1986-2000.
[5] Nat. Commun., 2015, 6,1-9. [6] Nat. Commun., 2023, 14, 1081.

Table S2. Physical properties of different electrolytes.

Sample	Composition (in mol ratio)	Ionic conductivity (mS cm^{-1} at 25 ℃)
Base-DEE	LiFSI:DEE:TTE=1:1:3	1.63
E-DEE	LiFSI:DEE:TTE=1:1.5:3	4.68
E-HDMN	LiFSI:DEE:HDMN:TTE=1:1:0.5:3	1.82
E-FDMN	LiFSI:DEE:FDMN:TTE=1:1:0.5:3	2.05

Table S3. Performance comparison of the practical thin Li||NMC cells using different electrolytes.

Electrolytes	Cathode	Anode	N/P ratio	Cut-off voltage (V)	Charging current density (A g⁻¹)	Cycling lifespan	Reference
LiFSI-1DEE-0.5FDMN-3TTE	NMC622	20 μm Li	2.5	4.5	0.2	250 cycles	This work
					0.4	175 cycles	
1 M LiFSI FDMB	NMC532	20 μm Li	2.5	4.2	0.066	210 cycles	[1]
LiFSI-1.8DME-2HFE-0.16TO	NMC532	50 μm Li	3.3	4.3	0.08	430 cycles	[2]
2 M LiFSI-TFDMP	NMC811	20 μm Li	4	4.3	0.1	200 cycles	[3]
2 M LiFSI-3BTFM-1DME	NMC811	20 μm Li	2.5	4.3	0.2	200 cycles	[4]
2 M LiFSI-DMP	NMC811	40 μm Li	3.4	4.3	0.4	160 cycles	[5]
1.2 M LiFSI/F5DEE or 1.2 M LiFSI/F4DEE	NMC811	50 μm Li	2	4.4	0.04	200 cycles	[6]
LiFSI-1.2DME-3TTE	NMC811	50 μm Li	2	4.4	0.066	155 cycles	[7]
LiFSI-1.2DME-3TFEO	NMC811	50 μm Li	6.7	4.4	0.066	300 cycles	[8]
0.9LiFSI-1DME-3HFC	NMC811	20 μm Li	2.7	4.4	0.1	800 cycles	[9]
5 M LiDFOB/DME-TTE	NMC811	45 μm Li	3.8	4.4	0.066	303 cycles	[10]
LiFSI-1DME-3NFS	NMC811	20 μm Li	1.2	4.4	0.04	200 cycles	[11]
1 M LiFSI-BFE	NMC811	50 μm Li	2.8	4.4	0.4	200 cycles	[12]

Reference:
[1] Nat. Energy, 2020, 5, 526-533. [2] Nat. Energy, 2023, 8, 725-735. [3] Nat. Commun., 2022, 13, 2575. [4] Chem, 2023, 9, 682-697.
[5] ACS Energy Lett., 2022, 8, 179-188. [6] Nat. Energy, 2022, 7, 94-106. [7] Joule, 2019, 3, 1662-1676. [8] Proc. Natl. Acad. Sci. USA. 118, e2020357118.
[9] Chem 9, 650-664. [10] Adv. Sci., 2021, 8, 2003240. [11] ACS Energy Lett., 2023, 8, 2868-2877. [12] Nat. Commun., 2022, 14, 1081.

Table S4. Parameters of the NMC811||Li pouch cell.

Cell component	Detials
Cathode	NMC811 with Al collector 12 pieces of double-side 2.3 mAh cm^{-2} for each-side
Seperator	PE
Anode	free-standing 50 μm Li for double side
N/P ratio	2.2
Size	73 mm×53 mm
Electrolyte	1.5 g Ah^{-1}
Discharge capacity	2.11 Ah
Midium voltage	3.82 V
Initial discharge energy	8156 mWh
Maximum charging power	7995 mW
Total cell weight	19.79 g
Entire cell energy density	412 Wh kg^{-1}
Maximum charging power density	404 W kg^{-1}

Table S5. Performance comparison of the practical high-energy-density pouch cells using different electrolytes.

Electrolytes	Cell capacity (Ah)	Cathode	Anode	N/P ratio	E/C ratio	Cut-off voltage (V)	Charging rate	Charging power density (W kg^{-1})	Energy density (Wh kg^{-1})	Cycling lifespan	Reference
LiFSI-1DEE-0.5FDMN-3TTE	2	NMC811	25 μm Li	2.2	1.5	4.4	1 C (2.30 mA cm^{-2})	404	412	120 cycles	This work
2 M LiFSI EGBE-TTE (1:1, v/v)	19	Ni90	60 μm Li	1.5	1.25	4.3	0.1 C (0.42 mA cm^{-2})	~57.5	505.9	130 cycles	[1]
1.02LiFSI-1DME-2PFB	6	NMC811	100 μm Li	3.8	1	4.4	0.2 C (0.42 mA cm^{-2})	~117	500	150 cycles	[2]
0.4 M LiTFSI THP + 20% FEC	0.1	NMC811	20 μm Li	1	0.96	4.2	0.2 C (0.76 mA cm^{-2})	~57.4*	474*	200 cycles	[3]
LiFSI-1.8DME-2HFE-0.16TO	5.3	NMC811	50 μm Li	1.8	2.1	4.3	0.1 C (0.56 mA cm^{-2})	~49.3	440	130 cycles	[4]
LiPF$_6$-LiNO$_3$-LiFEA-EC/DEC	0.42	NMC811	50 μm Li	2.7	2.8	4.3	0.4 C (1.46 mA cm^{-2})	~131.8	310	100 cycles	[5]
1.5 M LiFSI-DME-TTE	2	NMC622	20 μm Li	1	2.4	4.4	0.1 C (0.40 mA cm^{-2})	non-countable	350	501 cycles	[6]
1.5 M LiFSI/DME-MNBE	7.3	NMC811	50 μm Li	1.62	1.38	4.3	0.1 C (0.617 mA cm^{-2})	~56.9	503.7	100 cycles	[7]
1.2 M LiFSI-TEP-BTFE	1	NMC622	50 μm Li	2.6	3	4.4	0.1 C (0.38 mA cm^{-2})	~35.4	300	200 cycles	[8]
LiFSI-1DME-3NFS	0.42	NMC811	20 μm Li	0.93	3	4.4	0.2 C (0.86 mA cm^{-2})	~101.5*	440*	150 cycles	[9]
1 M LiFSI-BFE	0.3	NMC811	40 μm Li	2	2.4	4.4	0.2 C (0.80 mA cm^{-2})	~98.1*	426*	200 cycles	[10]

Note: * represents that the density calculations exclude the mass of tap and packing foil.

Reference:
[1] Nat. Energy, 2024, 9, 987-998. [2] Nat. Energy, 2024, 9, 1285-1296. [3] Nat. Energy, 2024, 9, 57-69. [4] Nat. Energy, 2023, 8, 725-735.
[5] Nat. Energy, 2023, 8, 934-945. [6] Nat. Energy, 2021, 6, 723-732. [7] Chem, 2024, https://doi.org/10.1016/j.chempr.2024.09.005. [8] Nat. Energy, 2019, 4, 551-559.
[9] ACS Energy Lett., 2023, 8, 2868-2877. [10] Nat. Commun., 2023, 14, 1081.

References

1. D. Ruan, L. Tan, S. Chen, J. Fan, Q. Nian, L. Chen, Z. Wang and X. Ren, *JACS Au* 2023, **3**, 953-963;

2. M. J. Frisch, G. W. Trucks, H. B. Schlegel, G. E. Scuseria, M. A. Robb, J. R. Cheeseman, G. Scalmani, V. Barone, G. A. Petersson, H. Nakatsuji, X. Li, M. Caricato, A. V. Marenich, J. Bloino, B. G. Janesko, R. Gomperts, B. Mennucci, H. P. Hratchian, J. V. Ortiz, A. F. Izmaylov, J. L. Sonnenberg, Williams, F. Ding, F. Lipparini, F. Egidi, J. Goings, B. Peng, A. Petrone, T. Henderson, D. Ranasinghe, V. G. Zakrzewski, J. Gao, N. Rega, G. Zheng, W. Liang, M. Hada, M. Ehara, K. Toyota, R. Fukuda, J. Hasegawa, M. Ishida, T. Nakajima, Y. Honda, O. Kitao, H. Nakai, T. Vreven, K. Throssell, J. A. Montgomery Jr., J. E. Peralta, F. Ogliaro, M. J. Bearpark, J. J. Heyd, E. N. Brothers, K. N. Kudin, V. N. Staroverov, T. A. Keith, R. Kobayashi, J. Normand, K. Raghavachari, A. P. Rendell, J. C. Burant, S. S. Iyengar, J. Tomasi, M. Cossi, J. M. Millam, M. Klene, C. Adamo, R. Cammi, J. W. Ochterski, R. L. Martin, K. Morokuma, O. Farkas, J. B. Foresman, D. J. Fox, Gaussian 16, Revision C.01, Gaussian, Inc., Wallin-Gaussian 16, Revision C.01, Gaussian, Inc., Wallin 2019.

3. K. G. Sprenger, V. W. Jaeger, J. Pfaendtner, *J. Phys. Chem. B* 2015, **119**, 5882-5895.

4. M. J. Abraham, T. Murtola, R. Schulz, S. Páll, J. C. Smith, B. Hess, E. Lindahl, GROMACS: *SoftwareX*, 2015, **1-2**, 19-25.